Received: 8 January 2025 | Revised: 24 February 2025 | Accepted: 26 February 2025

DOI: 10.1002/alz.70112

Alzheimer's & Dementia®
THE JOURNAL OF THE ALZHEIMER'S ASSOCIATION

RESEARCH ARTICLE

Neuronal ABCA7 deficiency aggravates mitochondrial dysfunction and neurodegeneration in Alzheimer's disease

Ni Wang[1] | **Yining Pan**[2] | **Skylar C. Starling**[1] | **Devon H. Haskell**[1] | **Astrid C. Quintero**[1] | **Keiji Kawatani**[1] | **Yasuteru Inoue**[1] | **Francis Shue**[1] | **Xiaoye Ma**[1] | **Tomonori Aikawa**[1] | **Yuka A. Martens**[1,3] | **Aishe Kurti**[1] | **Tammee M. Parsons**[1] | **Ralph B. Perkerson**[1] | **Bhaskar Roy**[1] | **Ana-Caroline Raulin**[1] | **Yingxue Ren**[4] | **Michael DeTure**[1] | **Dennis W. Dickson**[1] | **Hanmei Bao**[5] | **Xianlin Han**[5] | **Guojun Bu**[1,6] | **Takahisa Kanekiyo**[1]

[1]Department of Neuroscience, Mayo Clinic, Jacksonville, Florida, USA

[2]Department of Public Health, University of North Florida, Jacksonville, Florida, USA

[3]SciNeuro Pharmaceuticals, Rockville, Maryland, USA

[4]Department of Quantitative Health Sciences, Mayo Clinic, Jacksonville, Florida, USA

[5]Barshop Institute for Longevity and Aging Studies, University of Texas Health Science Center at San Antonio, San Antonio, Texas, USA

[6]Division of Life Science, The Hong Kong University of Science and Technology, Clear Water Bay Hong Kong, China

Correspondence
Takahisa Kanekiyo, Mayo Clinic, 4500 San Pablo Road, Jacksonville, FL. 32224, USA.
Email: kanekiyo.takahisa@mayo.edu

Funding information
NIH, Grant/Award Numbers: RF1AG081203 (to T.K.), U19AG069701 (to T.K.), R01AG071226 (to T.K.), RF1AG057181 (to T.K.), RF1AG068034 (to T.K.), RF1AG081203 (to X.H.), P30AG013319 (to X.H.), P30AG044271 (to X.H.), P30AG062677 (to D.W.D.); Cure Alzheimer's Fund (to T.K.)

Abstract

INTRODUCTION: Loss-of-function variants of the *ABCA7* gene are associated with an increased risk of Alzheimer's disease (AD). How neuronal ABCA7 contributes to AD pathogenesis is unknown.

METHODS: Using neuron-specific *Abca7* KO mice (n*Abca7*$^{-/-}$) with or without 5×FAD amyloid model background and *post mortem* AD brains, we investigated AD-related phenotypes through comprehensive approaches including transcriptomics and lipidomics.

RESULTS: Lipidomics analysis detected altered lipid profiles in the brains and synaptosomes of 5×FAD; n*Abca7*$^{-/-}$ mice compared to controls. Transcriptomics profiling revealed that neuronal ABCA7 deficiency altered the expression of genes and pathways related to mitochondrial homeostasis and apoptosis, particularly in excitatory neurons. Consistently, synaptosomes isolated from 5×FAD; n*Abca7*$^{-/-}$ mice showed diminished mitochondria respiration and reduced synaptic protein levels, which is further supported by results from human AD brains.

DISCUSSION: Our findings reveal that neuronal ABCA7 plays a critical role in mitochondrial homeostasis important for neuronal function and survival in the presence of AD pathology.

KEYWORDS
ABCA7, Alzheimer's disease, lipid, mitochondria, neuron

Highlights

- Neuronal ABCA7 deficiency exacerbates Aβ pathology and neuronal damage in 5×FAD mice.
- Neuronal ABCA7 deficiency alters brain transcriptomes and lipidomes of 5×FAD mice.
- Neuronal ABCA7 deficiency disturbs mitochondria functions in synaptosomes from 5×FAD mice.
- Neuronal *ABCA7* expression associates with genes and pathways related to mitochondrial homeostasis in AD brains.

1 | INTRODUCTION

Alzheimer's disease (AD) is a devastating neurodegenerative disease and is the most common form of dementia. It ranks as the sixth-leading cause of death in the United States.[1] Approximately 5% of AD cases are early onset, of which familial AD caused by mutations in *APP*, *PSEN1*, and *PSEN2* accounts for less than 15%.[2,3] While late-onset AD, which develops in individuals >65 years old, is more common, there is a heritability of 58% to 79%[4] in people with the *APOE* ε4 variant, the strongest genetic risk factor.[5] Recent genetic studies, including genome wide association studies (GWAS)[6] and meta-analyses,[7,8] have consistently identified *ABCA7* as a risk locus for AD. Of note, *ABCA7* loss-of-function variants are associated with an increased risk of both early-onset and late-onset AD.[9–13]

ABCA7 is a member of the ATP-binding cassette (ABC) transporter family, a group of highly conserved membrane proteins responsible for transporting substances across cellular membranes. Because ABCA7 and ABCA1 have a high amino acid similarity at 54%,[14] ABCA7 can mediate phospholipid and cholesterol efflux, thereby influencing the composition of brain lipids.[15] Whereas ABCA7 mainly functions in lipid metabolism, several studies indicate that the loss of ABCA7 contributes to elevated amyloid-β (Aβ) deposition in the brains of APP transgenic mouse models by facilitating APP processing and disturbing Aβ clearance.[16–18] ABCA7 deficiency has also been linked to altered immune responses in mouse models of AD.[19,20] ABCA7 haplodeficiency impaired proinflammatory responses in the brain after lipopolysaccharide injection.[19] ABCA7 deficiency affected ERK signaling in response to C1q or apoptotic cells and reduced phagocytic efficiency.[20] Moreover, a risk variant of *ABCA7* is associated with neuritic plaque formation in the human brain,[21] further supporting its role in AD pathology.

Our recent findings demonstrate that ABCA7 mediates lipid distribution from the endoplasmic reticulum (ER) to mitochondria and other cellular organelles in neurons.[22] The ER synthesizes most membrane lipids.[23] Mitochondria play pivotal roles in bioenergetic and metabolic processes. Mitochondria generate energy for cell metabolism through the tricarboxylic acid (TCA) cycle and oxidative phosphorylation (OXPHOS) via the electron transport chain (ETC) located in the inner mitochondrial membrane (IMM).[24] Research indicates that mitochondrial dysfunction is a key driver of AD pathogenesis.[25] In addition, patients with AD exhibit synaptic dysfunction or loss.[26] Because synapses depend heavily on mitochondria owing to their high energy demand for sustaining synaptic activity,[27] the interplay between mitochondria and synaptic health is crucial for understanding AD pathophysiology.

ABCA7 is expressed in neurons and other brain cell types.[17] A recent single-nucleus RNA (snRNA-seq) sequencing indicated that excitatory neurons (ExNs) exhibit the highest levels of *ABCA7* expression in human *post mortem* brains.[28] While *ABCA7* loss-of-function has been implicated in the etiology and pathology of AD, the underlying mechanism linking neuronal ABCA7 deficiency to AD pathogenesis remains elusive. Here, we report that the deletion of neuronal ABCA7 exacerbates brain Aβ accumulation and neurodegeneration accompanied by mitochondrial dysfunction in a novel neuronal *ABCA7* KO mouse model with amyloid pathology.

2 | METHODS

2.1 | Animals

We employed *Abca7* floxed mice,[22] established by Taconic Biosciences, through collaboration with the Cure Alzheimer's Fund. The *Abca7*-floxed mice ($Abca7^{floxp/floxp}$) were crossed with 5×$FAD^{+/-}$ mice[29] or Camk2a-$Cre^{+/-}$ mice[30,31] to generate the founders: 5×$FAD^{+/-}$; $Abca7^{floxp/floxp}$ mice and $Abca7^{floxp/floxp}$; Camk2a-$Cre^{+/-}$ mice (n$Abca7^{-/-}$). By breeding the mice, 5×$FAD^{+/-}$; $Abca7^{floxp/floxp}$; Camk2a-$Cre^{+/-}$ mice (5×FAD; n$Abca7^{-/-}$) were generated. The 5×$FAD^{+/-}$; $Abca7^{floxp/floxp}$; Camk2a-$Cre^{-/-}$ littermates were used as controls (5×FAD; control). Both male and female mice were subjected to experiments at 10 to 12 months old. All experimental animals were housed in a 12-h light-dark cycle at 25°C according to the National Institutes of Health (NIH) Guide for the Care and Use of Laboratory Animals. All animal experiments were approved by the Mayo Clinic Institutional Animal Care and Use Committee (A2822-17-R23).

2.2 | Participants

Datasets of snRNA-seq were obtained from the Religious Orders Study and Rush Memory and Aging Project (ROSMAP) (Table S1) and the

Seattle Alzheimer's Disease Brain Cell Atlas (SEA-AD) (syn26223298) (Table S2). Frozen tissues of frontal cortex from pathologically confirmed AD cases were provided by the Mayo Clinic Brain Bank for Neurodegenerative Diseases (Table S3).

2.3 | Behavioral tests

For elevated plus maze test, the apparatus consisted of two opposing open arms (50 × 10 cm) and two opposing closed arms with roofless gray walls (40 cm) connected by a central square platform and positioned 50 cm above the ground. Mice were placed in the open arms facing an open arm, and their behavior was tracked for 5 min by an overhead camera and analyzed by AnyMaze software.[32] For open field assay, animals were placed in an open field chamber (40 × 40 × 30 cm) for 15 min in standard room-lighting conditions. Movement of the mice in the chamber was captured by an overhead camera and analyzed by AnyMaze. The total traveled distance, average speed, and tracking time in the center (digitally designated by an 8 × 8 cm region) of the chamber compared to the perimeter were measured.[32] The fear conditioning test was conducted in a sound-attenuated chamber with a grid floor that delivered electric shocks. Freezing of the mice caused by the electric shocks was measured by an overhead camera and analyzed by the FreezeFrame software (Actimetrics). Mice were placed in the chamber without disturbance for 2 min and the baseline of mouse freezing behavior was recorded. The conditioned stimulus (CS), an 80-dB white noise, was presented for 30 s. The experimental mouse received an additional mild electric shock (0.5 mA) at the final 2 s of the noise, which was the unconditioned stimulus (US). After resting for 1 min, another round of the CS-US stimulation was performed on the mouse. After 30 s, the mouse was removed from the chamber. For contextual learning assessment, the mice were placed back in the training context 24 h after the training and monitored for freezing for 5 min. To examine the cued learning, the experimental mouse was placed in a different context (novel odor, cage floor, and visual cues) for 3 min. After that, the auditory CS was provided, and freezing was recorded for another 3 min. The freezing baseline was subtracted from the context or cued tests to exclude animal variability.[32] Morris water maze (MWM) was conducted in a pool (122 cm in diameter) filled with water mixed with non-toxic white paint at 21°C to 23°C, as described previously.[33] A transparent platform (10 cm in diameter) was placed in the target quadrant. Four different clues were placed on the sidewalls surrounding the tank, which were visible for the spatial orientation of the mice. For the visible platform test, the mice underwent one session of six pretraining trials where a visible marker was placed on the platform on day 1. For the hidden platform training, the platform was submerged 1.5 cm below the surface. Training sessions composed of six trials per day were performed on 3 consecutive days (days 2–4). For the probe test, the platform was removed, and the mice were placed at the opposite edge of the pool. Behaviors were monitored for 60 s on day 5. The swimming paths of mice were recorded by a video tracking system. The travel latencies, time spent in target quadrant, platform entries, and travel speed were analyzed by AnyMaze.

RESEARCH IN CONTEXT

1. **Systematic review**: AD is a devastating neurodegenerative disease and is the most common form of dementia. Recent genetic studies have consistently identified ABCA7 as a risk locus for AD. Of note, *ABCA7* loss-of-function variants are associated with an increased risk of both early-onset and late-onset AD. ABCA7 can mediate phospholipid and cholesterol efflux, thereby influencing the composition of brain lipids. Whereas ABCA7 mainly functions in lipid metabolism, several studies indicate that ABCA7 deficiency contributes to neuronal damage and exacerbates Aβ pathologies. We include these publications from in vitro and in vivo models as well as *post mortem* human brain samples.
2. **Interpretation**: The value of our study lies in investigating the roles of neuronal ABCA7 in AD pathogenesis in vivo. Neuronal ABCA7 compromises mitochondria and synapse functions in amyloid model mice and AD subjects by modulating lipid homeostasis.
3. **Future directions**: Our study suggests that interventions to restore ABCA7 function and lipid homeostasis in neurons hold promise as potential therapeutic strategies for AD. As ABCA7 is expressed in various brain cell types, future studies are needed to define the cell type-specific contributions of ABCA7 to AD-related phenotypes.

2.4 | Immunohistochemistry

Mouse hemispheres were fixed in 10% formalin and embedded in paraffin blocks. Samples were sectioned in 5-µm thickness and immunostained using the Dako Autostainer and EnVision+ Dual Link System-HRP (DAB+). The paraffin sections were incubated with primary antibodies for pan-Aβ, Iba1, glial fibrillary acidic protein (GFAP), and NeuN (Table S4) overnight at 4°C, followed by incubations with secondary antibodies (ABC kits, PK-6101 or PK-6102, Vector Laboratories) at room temperature for 1 h. Signals were developed using 3, 3-diaminobenzidine (DAB, SK-4100, Vector Laboratories) and scanned by the Aperio Slide Scanner (Leica Biosystems). The immune positivity was analyzed and quantified using Aperio ImageScope software (Leica Biosystems).

2.5 | Immunofluorescent staining

Mouse hemispheres were fixed in 4% paraformaldehyde (PFA) overnight at 4°C, followed by dehydration in 30% sucrose. The brain tissues were embedded in Tissue-Tek O.C.T. Compound (4583, Sakura). The frozen sections with 30-µm thickness were permeabilized with 0.5% Triton-X 100 in phosphate-buffered saline (PBS) for 5 min and blocked with 3% BSA at room temperature for 1 h. Sections were

incubated with primary antibodies (Table S4) overnight at 4°C, followed by incubations with corresponding fluorescently labeled secondary antibodies (A48255, A11004, A11001, A21235, A11008, A11011, A11006, A11077, or A31573, Invitrogen) and DAPI (D1306, Invitrogen). For X-34 (SML1954, Sigma-Aldrich) staining, sections were incubated with X34 in 40% ethanol/PBS at room temperature for 20 min. All images were captured by the Zeiss LSM 880 confocal microscope (Leica Biosystems). Fluorescence intensities were quantified with ImageJ software. Immunopositive area was quantified with Imaris 10.0.1 using surfaces. Plaque-associated Iba1-positive microglia, which surrounds X34-positive amyloid plaque within 15 μm, was quantified with Imaris using surface and plot. The sum of X34-positive amyloid plaque-associated LAMP1-positive area was quantified as the dystrophic neurites with Imaris using surface.

2.6 | In situ hybridization

In situ hybridization was performed using RNAscope Technology in the mouse frozen sections with 15-μm thickness (323110, Advanced Cell Diagnostics [ACD]). Briefly, the brain sections were baked at 65°C for 30 min and fixed in 4% PFA at 4°C for 15 min. After dehydration and drying, the slides were subjected to hydrogen peroxide incubation at room temperature for 10 min, boiled in the target retrieval buffer for 15 min, and incubated with RNAscope Protease III at 40°C for 15 min. The slides were incubated with ACD probes for *Abca7* (577991-O1, targeting NM_00134081.2 and NM_013850.2, region 1296-2328 bp) and *Rbfox3* (481701-C2; targeting NM_001285436.1, region 455-2954 bp), followed by amplification and signal development using fluorophore Opal 520 (OP-001001, Akoya Biosciences) or Opal 620 (OP-001004, Akoya Biosciences). Sections were counterstained with DAPI (ACD) and mounted with a Vectashield (H-1400, Vector Laboratories). Images were captured by the Zeiss LSM 880 confocal microscope.

2.7 | Western blotting

Samples were loaded onto a 4% to 20% precast polyacrylamide gel (5671095, Bio-Rad) and transferred onto PVDF membranes (1620177, Bio-Rad). The membranes were blocked with 5% non-fat milk and incubated with primary antibodies (Table S4) at 4°C overnight. Membranes were washed and incubated with secondary antibodies: HRP-conjugated anti-mouse or rabbit (ab 6728 or ab6721, Abcam). Membranes were subjected to stripping (2504, Millipore Sigma) when necessary. The immunoreactivities were detected by SuperSignal Substrate (34095, Thermo Fisher Scientific) through ChemiDoc imaging system (Bio-Rad). The blots were quantified by ImageJ software.

2.8 | RT-qPCR

The total RNAs were extracted from mouse cortices using an RNeasy Mini Kit (74106, QIAGEN), followed by cDNA synthesis using SuperScript III reverse transcriptase (18080051, Invitrogen). Real-time PCR was performed with SYBR Green Supermix (1725271, Bio-Rad), and relative gene expression was normalized to *Actb* expression and assessed using the $2^{-\Delta\Delta CT}$ method. Primers used in this study was summarized in Table S5.

2.9 | ELISA

Mouse brain samples were sequentially extracted in TBS, TBS-X, and GDN-HCl as described in a previous publication.[34] To capture human Aβx-40 or Aβx-42, mAb 13.1.1 and mAb 2.1.3 antibodies were used, respectively. The human Aβ1-16–specific mAb Ab5 antibody conjugated with HRP (ab274112, Abcam) was used as a detection antibody. The plates were developed with 3,3',5,5'-tetramethylbenzidine substrate (T5569, Sigma-Aldrich) and the reaction was stopped by 85% O-phosphoric acid. Colorimetric signals were measured at 450 nm using the Synergy HT plate reader (BioTek Instruments Inc).[18] For β-CTF measurement, the TBS-X fractions were used by following the manufacturer's protocol (27776, Immuno-Biological Laboratories [IBL]).[35] For oligomeric Aβ measurement, the TBS-X fractions were used by following the manufacturer's protocol (BEK-2215-1P, Biosensis). Colorimetric signals were measured at 450 nm using the Synergy HT plate reader (BioTek Instruments). The measured values were normalized by protein concentrations quantified using a BCA kit (23225, Thermo Fisher Scientific) in each fraction. In addition, mouse whole blood was harvested through the postcava with a 1-mL syringe and transferred to a collection tube containing EDTA (41.1395.105, Sarstedt), followed by centrifugation at 5000 rpm for 10 min at 4°C. Plasma levels of neurofilament light chain (NfL) were measured by a Simoa HD-1 analyzer (Quanterix) using NF-Light version 2 Advantage Kit (130186, Quanterix).

2.10 | Oxygen consumption rate measurement in synaptosomes

Mouse hemispheres were homogenized in Syn-PER reagent containing protease and phosphatase inhibitors (1861218, Thermo Fisher Scientific), and synaptosomes were isolated following the manufacturer's protocol. The synaptosome pellet was re-suspended in reagent containing protease and phosphatase inhibitors. For the oxygen consumption rate (OCR) measurement, 15 μg of synaptosomes in Syn-PER were plated on a 96-well microplate (101085, Agilent Technologies) precoated with poly(ethyleneimine) solution (03880, Sigma-Aldrich). After centrifugation at 3000 × g for 1 h at 4°C. The buffer was replaced with pre-warmed XF DMEM (103575-100, Agilent Technologies) in the microplate. A sensor cartridge (101085, Agilent Technologies) was incubated in pre-warmed XF Calibrant (103059-000, Agilent Technologies) at 37°C for 1 h. Oligomycin, FCCP, and Rot/AA (103015-100, Agilent Technologies) were diluted in XF DMEM containing glucose (103577, Agilent Technologies) and pyruvate (103578, Agilent Technologies). The diluted oligomycin (5 μM), FCCP (1 μM), and Rot/AA

(0.5 μM) were loaded in Ports A, B, and C of the sensor cartridge, respectively. The OCR was measured using the Seahorse XFe96 Analyzer (Agilent Technologies).

2.11 | Shotgun lipidomics

Shotgun lipidomics of brain hemispheres was performed as described previously.[18,36] In brief, lipids were extracted by the modified Bligh and Dyer method. A triple-quadrupole mass spectrometer equipped with a NanoMate device and Xcalibur system was used to analyze lipids. All mass spectrometry (MS) analyses were acquired by a customized sequence operated under Xcalibur software. Internal standards for quantification of individual molecular species of other lipid classes were added to each brain tissue sample at the start of the extraction procedure. Log2-transformed lipid compositions between two groups were compared by ANOVA. Differential lipid compositions were defined by p value <0.05 and |regression coefficient| (β) ≥ 0.1. The "pheatmap" (https://cran.r-project.org/web/packages/pheatmap) function was used to generate heatmap. Hierarchical clustering was based on the Euclidean distance metric and complete agglomeration method. Weighted correlation network analysis (WGCNA) in the lipidomics dataset was performed using the log2-transformed values of lipids after adjusting for sex and interaction between sex and genotype. Based on the relationship between power and scale independence, a power of 10, a minimum module size of five lipids for brains with 5×FAD background, a power of 6, a minimum module size of five lipids for brains without 5×FAD background, and a power of 10, a minimum module size of 10 lipids for synaptosomes, a minimum height for merging modules of 0.15 for brains with/without 5×FAD background and 0.2 for synaptosomes, and the "bicor" correlation function were used to build a signed network. Modules were annotated using LION/web (http://www.lipidontology.com/).[37] Lipids with high connectivity in the respective modules were considered hub lipids, which were visualized using VisANT.

2.12 | Bulk RNA-seq

The total RNAs were extracted from mouse cortices using an RNeasy Mini Kit (74106, QIAGEN). The RNA integrity number (RIN) was measured by the Agilent 2100 bioanalyzer. A total of 24 samples with 5×FAD background and 12 samples without 5×FAD background was sequenced using Illumina HiSeq 4000 at the Mayo Clinic. The reads were mapped to the mouse genome mm10, and raw gene read counts were generated using the Mayo Clinic RNA-seq analytic pipeline, MAP-RSeq.[38] Conditional quantile normalization (CQN) of the raw gene counts was used to correct for GC bias and gene length differences to obtain similar quantile-by-quantile distributions of gene expression levels across samples.[39] Based on the bimodal distribution of CQN-normalized and log2-transformed reads per kilobase per million (RPKM) gene expression values, genes with an average log2 RPKM of 1 or more in at least one group were considered to have been expressed above the detection threshold. Differential gene expression analyses were conducted using the *limma-trend* workflow.[40] Specifically, low expressed genes were removed using the "filterByExpr" function from edgeR.[41] Scaling factors for library size normalization were calculated by "calcNormFactors" function with method = "TMM." For samples with 5×FAD background, the models were adjusted for sex and RIN, which were a significant source of variation in the gene expression values (mean F ratio > 1.5). Differentially expressed genes (DEGs) were defined by |fold change| ≥ 1.2 and Benjamini–Hochberg adjusted p value < 0.05. Heatmaps showing the expression values of selected genes affected by genotypes were generated by the "pheatmap" function. The gene expression values affected by genotype were calculated using the "removeBatchEffect" function from the limma package to remove the impacts of sex and RIN.[42] For samples without 5×FAD background, the models were adjusted for sex, which was a significant source of variation in the gene expression values (mean F ratio > 1.5). DEGs were defined by |fold change| ≥ 1.2 and p value < 0.05.

2.13 | Cell type deconvolution

We leveraged a public single-cell RNA (scRNA-seq) dataset of mouse model to deconvolve gene signature patterns of our RNA-seq data from mouse cortex.[43] The analysis process was adapted from a published protocol.[44] Briefly, neurons and non-neurons (Astro, Micro-PVM, Oligo, VLMC, SMC_Peri, and Endo) from cortex in the scRNA-seq dataset were subset. Then we filtered genes expressed in our RNA-seq by significance (p <0.01) and ranked them by fold change. By intersecting the gene list in our dataset and genes from the reference scRNA-seq dataset, we used the top or bottom 1166 DEGs in the KO group for further analysis. Based on the normalized and scaled expression values of the selected genes, we used the Seurat package (version 5.0.1) to conduct stochastic nearest neighbors (tSNE) non-linear dimensionality reduction.[45]

2.14 | Gene set enrichment analysis of mouse transcriptome

Gene set enrichment analysis (GSEA) was conducted using the clusterProfiler package[46] for "enriched" Gene Ontology (GO) and Reactome annotation gene sets. In GSEA, genes were pre-ranked using the formula sign (fold change) × − log10(P). The downregulated or upregulated GO terms as well as Reactome pathways were visualized using R (version 3.6.3).

2.15 | WGCNA in mouse brain transcriptomes

WGCNA was performed using CQN-normalized and log2-transformed RPKM values adjusted for RIN and sex.[47] A signed hybrid

co-expression network was built. Based on the relationship between power and scale independence, the power of 10 or 22 was chosen to build scale-free topology of samples with/without 5×FAD background using signed hybrid network. Hybrid dynamic tree cutting was used based on a minimum module size of 60 genes and a minimum height for merging modules of 0.15 or 0.3 (with or without 5×FAD background) and "bicor" correlation function. Each module was summarized by ME and assigned a unique color identifier; genes that did not fulfill criteria for any of the modules were assigned to the gray module. Modules were annotated using WGCNA R package anRichment. Genes with high connectivity in the respective modules were considered hub genes. Gene-gene connections among top hub genes were visualized using VisANT.

2.16 | Mouse brain snRNA-seq

Single nucleus RNAs isolated from frozen mouse hemispheres were lysed in cold lysis buffer (10 mM Tris-HCl, 10 mM NaCl, 1 mM MgCl2, 0.1% IGEPAL, and 300 U/mL RNase inhibitor), followed by filtering using a 100-µm strainer and centrifugation at 500 × g and 4°C for 5 min. Samples were washed with cold 20 mg/mL BSA in PBS and filtered by a 40-µm strainer and centrifugated 500 × g and 4°C for 5 min. Nuclei were resuspended in cold 20 mg/mL BSA in PBS. The isolated nuclei were quantified using a hemocytometer and fixed using a nucleus fixation kit from Parse Biosciences according to the manufacturer's protocol. Then the fixed single nuclei were barcoded with the Evercode WT mini version 2 kit (ECW02010, Parse Biosciences) from Parse Biosciences, and libraries were prepared (ECW02010, Parse Biosciences) according to the manufacturer's instructions. Data were pre-processed using the default settings of the Parse Biosciences pipeline, including demultiplexing samples, aligning reads to the GRCm38 mouse genome, and performing quality control. Downstream analyses were performed using the R package Seurat (version 4.0.2) at the default settings unless otherwise noted. The gene–cell matrix was normalized and scaled using Seurat's "NormalizeData" and "ScaleData" functions, and principal component analysis (PCA) was performed with Seurat's "RunPCA" function; cells were clustered using the "FindNeighbors" (30 dimensions of reduction) and "FindClusters" (resolution = 0.8) functions; for visualizing clusters, "RunUMAP" (30 dimensions) was run. Logistic regression tests were performed to determine DEGs between clusters using the "FindConservedMarkers" function. The identity of cell clusters was determined manually using datasets for murine cell taxonomy.[43] Three clusters of non-neurons were characterized further using Seurat's "subset" function (resolution = 1.2). Ambiguous cells with expression of distinct lineage markers were deemed to be likely multiplets and were labeled as mixed cell types. Cell annotations for the remaining clusters were conducted manually and added to the main dataset. In total, filtering low-quality and ambiguous cells resulted in 3776 cells, including 813 mixed cells for analysis. DEGs in the ExN clusters between two groups were determined using a pseudobulk approach by the "pseudobulkDGE" function from the scran package.[48] Briefly, all the cells in each ExN cluster in each sample were pooled computationally by summing all counts for a given gene. DEGs were determined by the method = "edgeR." Models were controlled for sex and number of cells in the cluster. Sex was modeled as a two-level factor variable, and the number of cells in clusters was modeled as continuous variable. GO analysis (hypergeometric test) of upregulated and downregulated marker genes in ExNs was performed using Metascape (http://metascape.org/).[49] Semantic similarity analysis and visualization of the enriched GO terms were conducted by REVIGO (http://revigo.irb.hr/).[50] GO analysis (hypergeometric test) of upregulated and downregulated marker genes in ExNs was performed using the "enrichGO" function in the clusterProfiler package.[46]

2.17 | Analysis in snRNA-seq dataset from AD brains

The *post mortem* human brain snRNA-seq dataset from 27 cases diagnosed as "Alzheimer's dementia" with *APOE* ε3/ε3 and Braak V-VI was sourced from the Religious Order Study (ROS) or the Rush Memory and Aging Project (MAP) (ROSMAP).[51] Based on the cell type information provided by the dataset of the prefrontal cortex, we calculated the expression levels of *ABCA7* in both excitatory and inhibitory neurons (InN) through a pseudobulk RNA-seq. Based on expressions of *ABCA7* and to ensure balanced distribution of sex between groups, we included cases with the highest *ABCA7* expressions ($N = 6$) and the lowest *ABCA7* expressions ($N = 6$) (Table S1). Pre-processing and downstream analyses were conducted using the Seurat package (5.0.1).[45] All the samples were integrated, and a harmony method was performed to identify common sources of variation and to remove batch effects. The first 30 principal components were used for subsequent clustering analysis and UMAP visualization dimension. Clusters were identified with "FindClusters" using a resolution parameter of 0.8. The annotation of each cluster was manually performed using the Allen Brain Map portal - Human Multiple Cortical Areas SMART-seq taxonomy (https://portal.brain-map.org/atlases-and-data/rnaseq/human-multiple-cortical-areas-smart-seq). DEGs in the excitatory and inhibitory neuron clusters between the two groups were determined using a pseudobulk approach by the "pseudobulkDGE" function from the scran package.[48] Models were controlled for sex, years of education, and number of cells in the cluster, as the years of education significantly affected gene expression in the data (mean F ratio > 1.2). GSEA was conducted using the clusterProfiler package[46] for "enriched" GO and Reactome annotation gene sets. In GSEA, genes were pre-ranked using the formula sign (fold change) × −log10(*P*). The downregulated or upregulated GO terms were visualized using R version 3.6.3.

The brain snRNA-seq dataset from 27 cases diagnosed as "Alzheimer's disease, dementia" with Braak V-VI was obtained from the SEA-AD cohort (syn26223298). Based on the cell type information provided by the dataset of prefrontal cortex, we calculated the expression levels of *ABCA7* in both excitatory and InN through a pseudobulk RNA-seq. Cases with the highest *ABCA7* expressions (N = 10) and the lowest *ABCA7* expressions (N = 10) were included in this study (Table S2). Function "emptyDrops" from the DropletUtils package was used

to filter out empty droplets in the downloaded raw feature-barcode matrix files.[52] Pre-processing and downstream analyses were conducted using Seurat package (5.0.1).[45] For quality control, cells that had unique gene counts >4,000 or <500 and > 20% mitochondrial content were removed. All the samples were integrated, and harmony method was performed to identify common sources of variation and to remove batch effects. The first 20 principal components were used for subsequent clustering analysis and UMAP visualization dimension. Clusters were identified with "FindClusters" with a resolution parameter of 0.4. Function "FindConservedMarkers" was used to determine cluster-specific genes that were conserved across conditions. The annotation of each cluster was manually performed using the Allen Brain Map portal - Human Multiple Cortical Areas SMART-seq taxonomy (https://portal.brain-map.org/atlases-and-data/rnaseq/human-multiple-cortical-areas-smart-seq). DEGs in the ExN clusters between the two groups were determined using pseudobulk approach by the "pseudobulkDGE" function from scran package.[48] Briefly, all the cells in each ExN cluster in each sample were pooled computationally by summing all counts for a given gene. DEGs were determined by the method = "edgeR." Models were controlled for sex, RIN, *APOE4* status, and number of cells in the cluster. Sex and *APOE4* status were modeled as two-level factor variables, and RIN and number of cells in the cluster were modeled as continuous variables. GO analysis (hypergeometric test) of upregulated and downregulated marker genes in ExNs was performed using Metascape (http://metascape.org/).[49] Semantic similarity analysis and visualization of the enriched GO terms were conducted by REVIGO (http://revigo.irb.hr/).[50]

2.18 | Statistics

All statistical analyses were performed with GraphPad Prism software or R (version 3.6.3). Statistical details of the experiments, including sample sizes and statistical tests, are described in the figure legends. Results are displayed as mean ± SEM. Mean values for groups were compared using two-way ANOVA and Tukey HSD test or two-tailed unpaired Student *t* test. $P < .05$ was considered statistically significant.

3 | RESULTS

3.1 | Increased brain Aβ accumulation in the neuronal ABCA7 deficient 5×FAD mice

We generated neuron-specific ABCA7 KO mice (n*Abca7*$^{-/-}$) by crossing *Abca7* floxed mice with *Camk2a*-Cre mice.[22] To elucidate how neuronal ABCA7 contributes to the pathogenesis of AD, we crossed the mice with 5×FAD mice and generated a neuron-specific ABCA7 KO mouse model with amyloid pathology (5×FAD; n*Abca7*$^{-/-}$). Through immunostaining or in situ hybridization, we confirmed the specific deletion of neuronal ABCA7 in the cortex (Figure S1) and hippocampus (Figure S2) of 10-month-old 5×FAD; n*Abca7*$^{-/-}$ mice.

To examine the effect of ABCA7 deletion in neurons on Aβ pathology, we performed immunohistochemical analysis using a pan-Aβ antibody in brain slices from 5×FAD; n*Abca7*$^{-/-}$ and littermate 5×FAD; control mice at 10 to 12 months of age (Figure 1A). We found greater Aβ burden in the cortex of 5×FAD; n*Abca7*$^{-/-}$ mice than in those of the control groups (Figure 1B), while a significant difference was not detected in the hippocampus (Figure 1C). We next sequentially extracted proteins from the cortex and hippocampus of 10-month-old mice using Tris-buffered saline (TBS), 1% Triton X in TBS (TBS-X), and guanidine hydrochloride (GDN-HCl) and measured Aβ40 and Aβ42 levels in each fraction by ELISA (Table S6). Consistent with the results of the immunostaining, both Aβ40 and Aβ42 levels in the soluble TBS fraction (Figure 1D), detergent-soluble TBSX fraction (Figure 1E), and detergent-insoluble GDN-HCl fraction (Figure 1F) were increased in the cortex of 5×FAD; n*Abca7*$^{-/-}$ mice. In addition, we also found higher levels of the β C-terminal fragment of APP (β-CTF) and oligomeric Aβ in the cortex of 5×FAD; n*Abca7*$^{-/-}$ mice than in that of the controls (Figure S3). While TBS-soluble Aβ40 and Aβ42 levels were not affected by neuronal ABCA7 deficiency in the hippocampus (Figure 1G), TBSX-soluble Aβ42 (Figure 1H) and insoluble Aβ40 and Aβ42 were increased in 5×FAD; n*Abca7*$^{-/-}$ mice (Figure 1I). Together, these results indicate that the deletion of ABCA7 in neurons exacerbates brain Aβ accumulation in 5×FAD mice, especially in the cortex, possibly by facilitating Aβ production and aggregation. We observed no evident difference in Aβ burden in 5×FAD; n*Abca7*$^{-/-}$ mice versus the control mice at 3 to 4 months of age (Figure S4).

3.2 | Exacerbated neuronal damage in neuronal ABCA7-deficient 5×FAD mice

When neurobehavioral tests were performed in the cohorts of n*Abca7*$^{-/-}$ mice and controls with or without 5×FAD background at 10 to 12 months of age, we found that neuronal ABCA7 deficiency exacerbated anxiety-related phenotypes as assessed by the elevated plus maze test in the 5×FAD mice (Figure S5A). In the open field test, n*Abca7*$^{-/-}$ mice showed significantly reduced exploratory activity compared to the control group without amyloid pathology (Figure S5B). Evident differences were not induced by neuronal ABCA7 deficiency in the fear conditioning test (Figure S5C–D) and MWM test (Figure S5E–H) in the mice regardless of amyloid pathology.

To assess the effect of neuronal ABCA7 deficiency on neuritic dystrophy, amyloid plaques were stained using X34 dye, and dystrophic neurites were stained using a LAMP1 antibody in brain slices from 5×FAD; n*Abca7*$^{-/-}$ and littermate 5×FAD control mice at 10 to 12 months of age (Figure 2A). Increased trends in X34-positive areas were observed in the cortex (Figure 2B) and hippocampus (Figure 2C) of 5×FAD; n*Abca7*$^{-/-}$ mice compared to controls. We found significant increases in the LAMP1-positive area and the X34-associated LAMP1 area in the cortex of 5×FAD; n*Abca7*$^{-/-}$ mice (Figure 2B), indicating exacerbated neuritic dystrophy. No evident difference in neuritic dystrophy between the groups was detected at the age of 4 to 5 months (Figure S6A–C). While lower microglial coverage of amyloid plaques

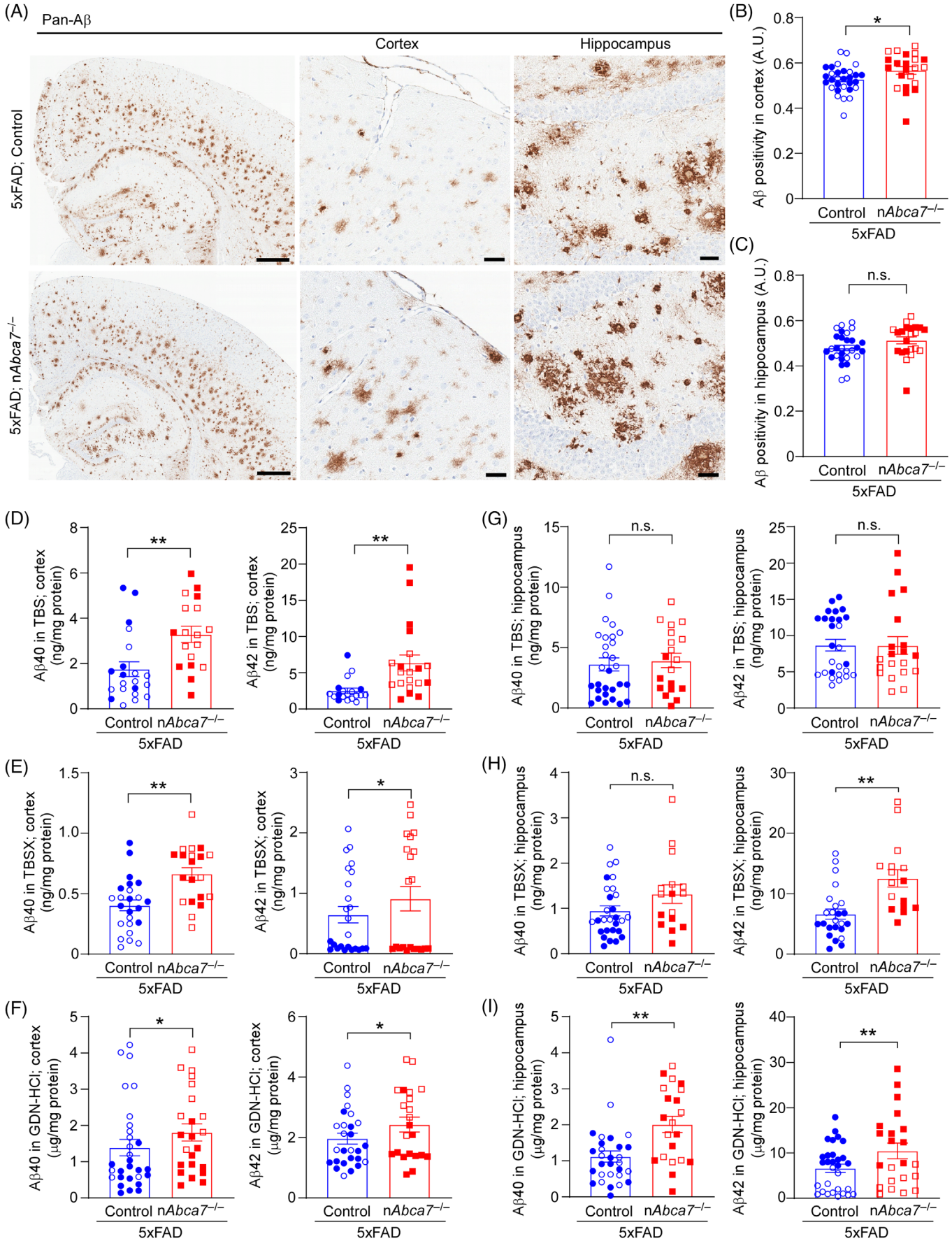
(A)
Pan-Aβ
Cortex
Hippocampus
5xFAD; Control
5xFAD; nAbca7−/−
(B)
Aβ positivity in cortex (A.U.)
*
Control
nAbca7−/−
5xFAD
(C)
Aβ positivity in hippocampus (A.U.)
n.s.
(D)
Aβ40 in TBS; cortex (ng/mg protein)
Aβ42 in TBS; cortex (ng/mg protein)
**
(E)
Aβ40 in TBSX; cortex (ng/mg protein)
Aβ42 in TBSX; cortex (ng/mg protein)
**
*
(F)
Aβ40 in GDN-HCl; cortex (μg/mg protein)
Aβ42 in GDN-HCl; cortex (μg/mg protein)
*
(G)
Aβ40 in TBS; hippocampus (ng/mg protein)
Aβ42 in TBS; hippocampus (ng/mg protein)
n.s.
(H)
Aβ40 in TBSX; hippocampus (ng/mg protein)
Aβ42 in TBSX; hippocampus (ng/mg protein)
n.s.
**
(I)
Aβ40 in GDN-HCl; hippocampus (μg/mg protein)
Aβ42 in GDN-HCl; hippocampus (μg/mg protein)
**

FIGURE 1 Neuronal ABCA7 deficiency accelerates brain Aβ accumulation in 10- to 12-month-old 5×FAD mice. (A–C) Quantification of Aβ positivity through immunostaining using pan- Aβ antibody in the cortex (B) and hippocampus (C) in 5×FAD control (male, $N = 16$; female, $N = 14$) and 5×FAD; n*Abca7*$^{-/-}$ mice (male, $N = 12$; female, $N = 10$). Scale bars, 500 μm (left) and 50 μm (middle and right) (A). (D–I) Aβ42 and Aβ40 amounts measured by ELISA in TBS, TBSX, and GDN-HCl fractions of the cortex (D–F) and hippocampus (G–I) from 5×FAD control (male, $N = 5$ to 16; female, $N = 12$ to 14) and 5×FAD; n*Abca7*$^{-/-}$ mice (male, $N = 7$ to 12; female, $N = 9$ or 10). Data are shown in mean ± SEM. Open and closed symbols indicate female and male mice, respectively. $^{*}p < 0.05$, $^{**}p < 0.01$, and n.s. by two-way ANOVA test after adjusting for sex. Aβ, amyloid beta; GDN-HCl, guanidine hydrochloride; n.s., not significant; TBS, tris-buffered saline; TBSX, Triton X in TBS.

has been associated with more severe axonal dystrophy,[53] there were no differences in the MG coverage of each amyloid plaque based on Iba1-positive staining between the two groups of mice (Figure S7). We next investigated whether neuronal ABCA7 deficiency influenced lipophagy by assessing colocalization of LAMP1- and NileRed-positive lipid droplets in 5×FAD mice. While we observed trends of increase in the cortex and hippocampus of 5×FAD; n*Abca7*$^{-/-}$ mice compared to controls, there were no significant differences (Figure S8).

In addition, Western blotting revealed a significant reduction in presynaptic synaptophysin (SYP) and a trend toward decreased postsynaptic PSD95 levels in the cortex of 5×FAD; n*Abca7*$^{-/-}$ mice compared to controls at 10 to 12 months of age (Figure 2D-E), but not at 4 to 5 months of age (Figure S6D–E). Consistent with these results, we also found higher plasma levels of NfL in 5×FAD; n*Abca7*$^{-/-}$ mice than in controls (Figure 2F), which is an established axonal degeneration marker.[54] These findings indicate that neuronal ABCA7 deficiency aggravates Aβ-induced neurodegeneration. In addition, we examined the effects of neuronal ABCA7 deficiency on glial cells using immunostaining. While we did not observe evident differences in Iba1 and GFAP positivity between the groups, higher Iba1 positivity was observed in the hippocampus of 5×FAD; n*Abca7*$^{-/-}$ mice than in controls (Figure S9). Damaged myelin basic protein (dMBP) levels were increased in the

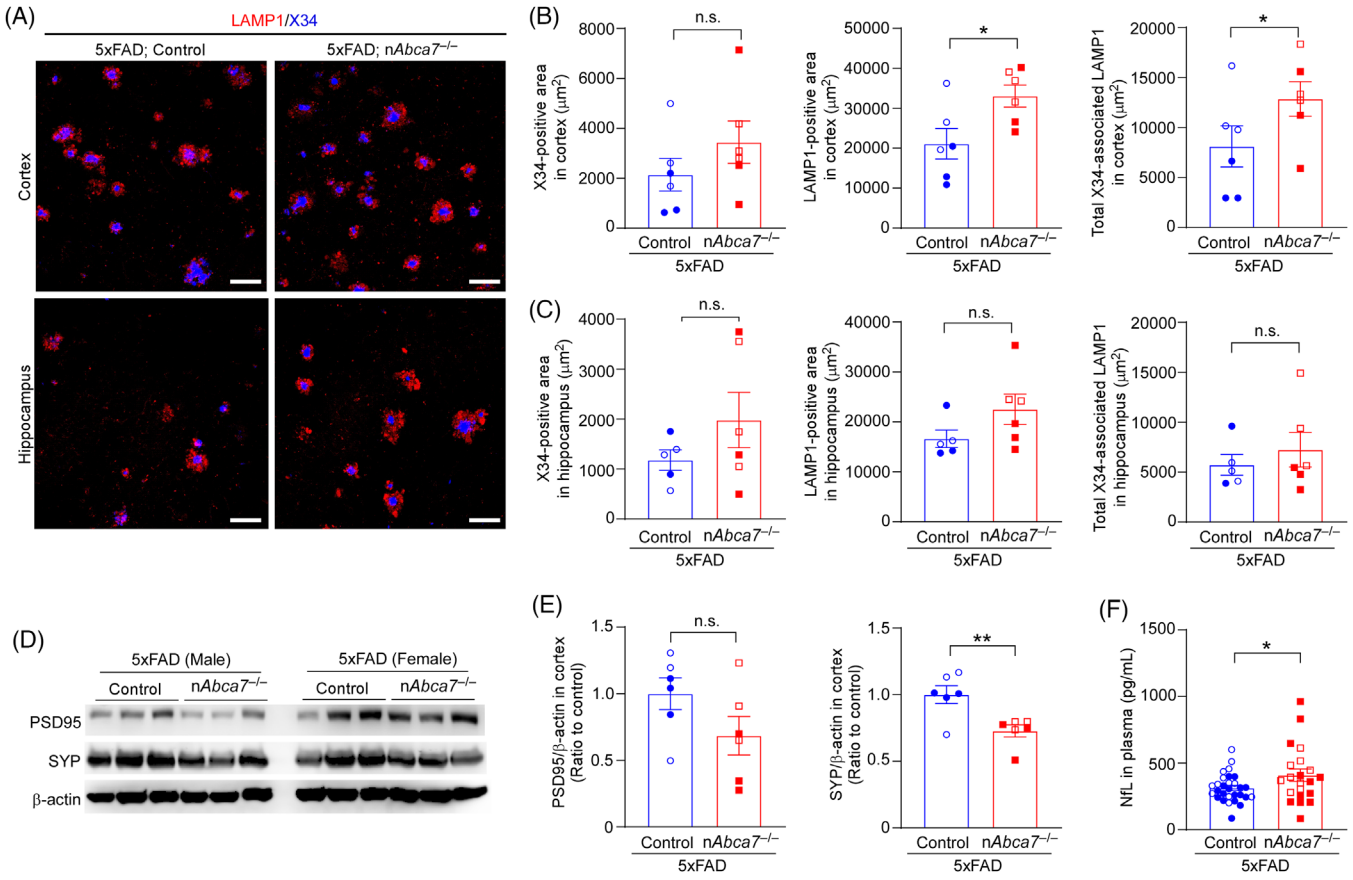

FIGURE 2 Neuronal ABCA7 deficiency exacerbates neuronal damage in 10- to 12-month-old 5×FAD mice. (A–C) Quantification of X34-positive or LAMP1-positive area and total X34-associated LAMP1 area in the cortex (B) and hippocampus (C) of 5×FAD; control (male, $N = 2$ to 3; female, $N = 3$) and 5×FAD; n*Abca7*$^{-/-}$ mice (male, $N = 3$; female, $N = 3$). Scale bars, 50 μm. (D and E) Quantification of PSD95 and SYP by Western blotting in t cortex from 5×FAD control (male, $N = 3$; female, $N = 3$) and 5×FAD; n*Abca7*$^{-/-}$ mice (male, $N = 3$; female, $N = 3$). (F) NfL levels measured by Quanterix Simoa NfL assay kit in plasma from 5×FAD control (male, $N = 16$; female, $N = 13$) and 5×FAD; n*Abca7*$^{-/-}$ mice (male, $N = 12$; female, $N = 9$). Data are shown in mean ± SEM. Open and closed symbols indicate female and male mice, respectively. $^{*}p < 0.05$, and n.s. by two-way ANOVA test after adjusting for sex. NfL, neurofilament light; n.s., not significant; SYP, synaptophysin.

cortex of 5×FAD; n*Abca7*$^{-/-}$ mice when normalized to the positivity of the neuronal marker Tuj1 (Figure S10), indicating exacerbated myelin damage.

3.3 | Lipid alterations in brains of neuronal ABCA7-deficient 5×FAD mice

To investigate the role of neuronal ABCA7 in brain lipid metabolism, we performed shotgun lipidomics in the brains of 5×FAD; n*Abca7*$^{-/-}$ mice and littermate 5×FAD control mice at 10 to 12 months of age. PCA showed a clear separation of lipid profiles between the two groups of mice (Figure 3A). Fourteen lipids, including subclasses of cardiolipin (CL) and phosphatidylcholine (PC), were upregulated ($p < 0.05$) in 5×FAD; n*Abca7*$^{-/-}$ mice compared to 5×FAD control mice, whereas 18 lipids, including lysophosphatidylethanolamine (LPE) species, were downregulated (Figure 3B). WGCNA of lipidomics results identified one downregulated module (MEtan) and one upregulated module (MEblack) (Table S7). MEtan was enriched for LPE subclasses (Figure 3C), where "*positive intrinsic curvature*" and "*fatty acid with 22-24 carbons*" were top-ranked GO terms (Figure 3D). In MEblack, the top 10 hub lipids included PC and PE (Figure 3E), and "*neutral intrinsic curvature*" was identified as the top-ranked pathway as well as "*fatty acid with 16-18 carbons*" (Figure 3F). These results suggest that ABCA7 modulates membrane phospholipid compositions depending on their acyl chain lengths and alters membrane curvature or structure in neurons. While ER is a critical organelle for lipid synthesis, immunostaining found that ABCA7 was mainly colocalized with the ER marker KDEL in the cortex (Figure 3G) and hippocampus (Figure 3H) of the mice, suggesting a contribution of ABCA7 to lipid metabolism in ER. We also investigated lipidomes in the brains of n*Abca7*$^{-/-}$ mice and the controls without amyloid pathology at 10 to 12 months old. PCA detected a clear separation in the lipidomes between the groups (Figure S11A), where total levels of CL, PA, PG, PI, and PS were significantly lower in n*Abca7*$^{-/-}$ mice than the controls (Figure S11B). Among 47 differentially expressed lipids, most of them were downregulated by neuronal ABCA7 deficiency, including CL and PG subspecies (Figure S11C). The WGCNA identified four downregulated modules (MEturquoise, MEgreenyellow, MEbrown, and MEmidnightblue) enriched for CL, PG, and PA subspecies in n*Abca7*$^{-/-}$ mice compared to the controls, while MEsalmon enriched for LPE with saturated acyl chains was upregulated (Figure S11D–H and Table S8). These results indicate that neuronal ABCA7 deficiency substantially influences brain lipid metabolism, which may be differently modulated by the presence of amyloid pathology.

3.4 | Altered brain transcriptomes in the neuronal ABCA7 deficient 5×FAD mice

To examine the effect of neuronal ABCA7 deficiency on brain transcriptomes, we conducted bulk RNA-seq of cortical samples from 5×FAD; n*Abca7*$^{-/-}$ and littermate 5×FAD control mice at 10 to 12 months of age. We identified 98 DEGs filtered by |fold change| ≥ 1.2 and adjusted p value <0.05 (Table S9), which included genes related to synaptic function (*Rimbp2*, *Grin2a*, *Slc6a7*, and *Syt2*) and lipid metabolism, especially fatty acid metabolism (*Abcd1*, *Acbd7*, *Dbi*, *Gpam*, *Zdhhc23*, and *Ndufab1*) (Figure 4A). When the bulk RNA-seq data were deconvoluted into brain cell types, the tSNE plot showed that excitatory and inhibitory neurons were the most abundant cell types with different distributions between the two groups (Figure 4B). Consistently, the scRNA-seq database in the frontal cortex of adult mice has shown that *Abca7* expression is high in *Fezf2*–, *Parm1*–, or *Syt6*-positive excitatory neurons in layers 5 and 6 and *Sst*– and *Pvalb*-positive inhibitory interneurons.[55] GSEA revealed that GO terms related to synaptic potential and synaptic vesicle fusion were upregulated in 5×FAD; n*Abca7*$^{-/-}$ mice (Figure 4C and Table S10), whereas downregulated GO terms included pathways related to mitochondrial respiratory chain complex assembly and ATP synthesis (Figure 4D). In addition, WGCNA identified two downregulated modules (MEturquoise and MEyellow) and two upregulated modules (MEbrown and MEmidnightblue) in 5×FAD; n*Abca7*$^{-/-}$ mice compared with the controls (Table S11 and S12). In MEturquoise, *Vapa*, *Rab6a*, *Rab1a*, and *Rab14* were identified as hub genes (Figure 4E) and were enriched for GO terms related to intracellular structure and membrane-bounded organelle (Figure 4F). Hub genes in MEyellow included *Suclg1*, *Mpc2*, *Mrpl13*, and *Ndufb5* (Figure 4G). *Suclg1* encodes a subunit of succinyl-CoA ligase that targets the mitochondria and converts ADP/GDP into ATP/GTP. Mutations in *Suclg1* may result in mitochondrial DNA depletion.[56] Mitochondrial pyruvate carrier 2, encoded by *Mpc2*, is associated with early-onset mitochondriopathy caused by disrupted mitochondria pyruvate metabolism.[57] *Mrpl13* and *Ndufb5* are involved in mitochondrial protein synthesis and the mitochondrial respiratory chain, respectively.[58,59] The GO terms in MEyellow were also related to the mitochondrial membrane and envelope (Figure 4H). The hub genes in MEbrown included *Gabrb2*, *Slc12a6*, *Atp2b3*, *Stxbp5l*, *Kcnk9*, *Kcnma1*, and *Kcan2* (Figure 4I), which are associated with cytosolic translation and ribosomal activity (Figure 4J). In MEmidnightblue, *Slc27a1* and *Aifm3* were identified as hub genes (Figure 4K). While SLC27A1 contributes to fatty acid metabolism by transporting long-chain fatty acids across the plasma membrane,[60] AIFM3 is involved in programmed cell death via mitochondrial depolarization, cytochrome c release, and caspase-3 activation.[61] "*Nuclear protein-containing complex*" was one GO term identified with a significant adjusted p value in the module (Figure 4L).

In addition, we also performed bulk RNA-seq in the brains of n*Abca7*$^{-/-}$ and littermate control mice without amyloid pathology at 10 months of age. We found 482 DEGs filtered by |fold change| ≥ 1.2 and $p < 0.05$ (Figure S12A and Table S13). GSEA revealed that GO terms related to ATP synthesis were upregulated by neuronal ABCA7 deficiency, whereas those related to synaptic membrane were downregulated (Figure S12B and Table S14). Although it conflicts with the result from the mice with amyloid pathology, genes related to ATP synthase may be upregulated as a compensation mechanism to ameliorate mitochondria dysfunction due to neuronal ABCA7 deficiency. Furthermore, WGCNA identified one downregulated module (MElightyellow)

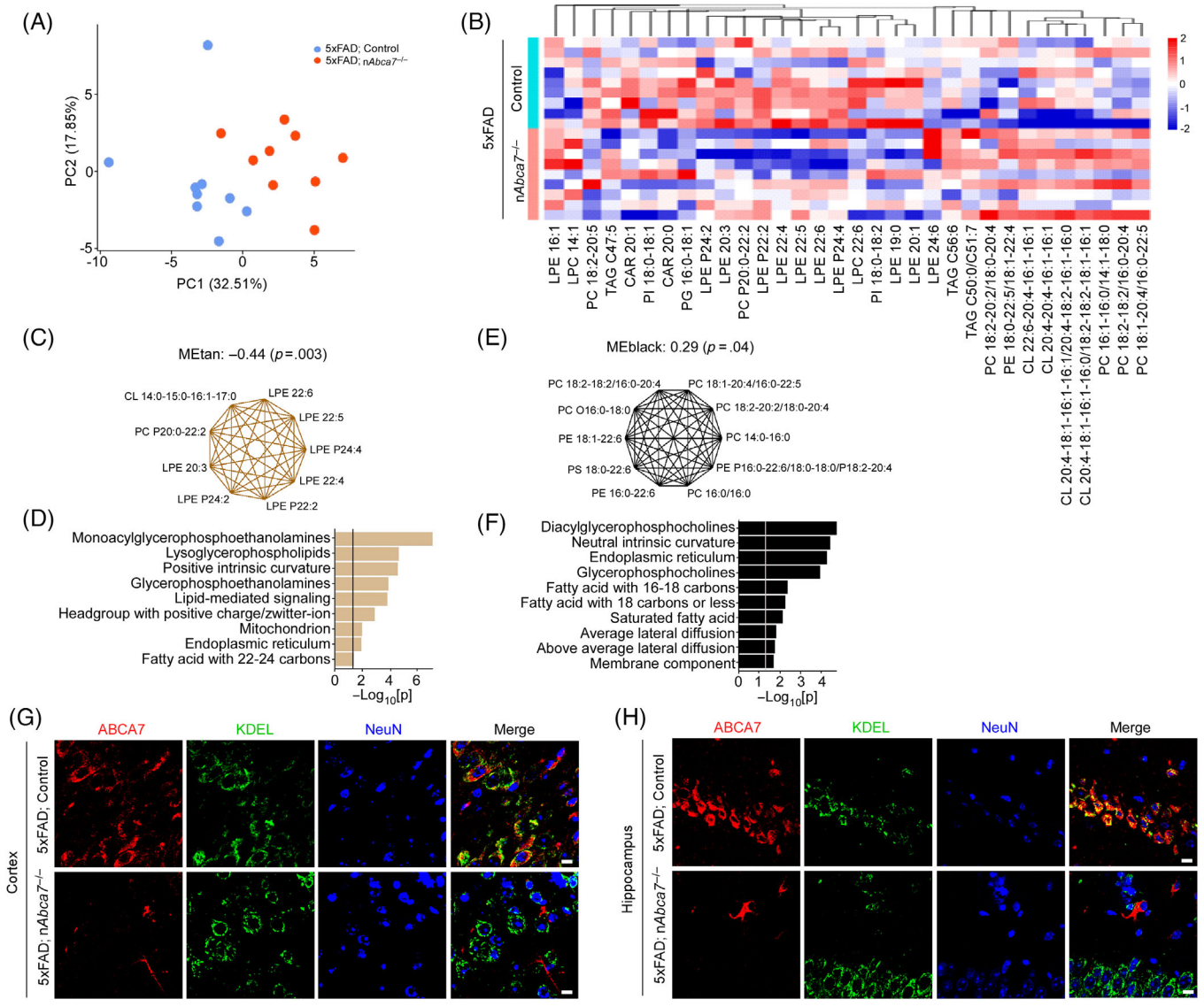

FIGURE 3 Neuronal ABCA7 deficiency alters brain lipid profiles in 10-month-old 5×FAD mice. (A) PCA in lipidomics dataset of brains from 5×FAD control (male, $N = 4$; female, $N = 5$) and 5×FAD; n*Abca7*$^{-/-}$ mice (male, $N = 4$; female, $N = 5$). (B) Hierarchical clustering of the 14 upregulated and 18 downregulated differentially expressed lipids with $p < 0.05$ by two-way ANOVA after adjusting for sex. (C–F) WGCNA in the lipidomics dataset with one MEtan and one MEblack comparing 5×FAD; n*Abca7*$^{-/-}$ mice with 5×FAD control mice. Top-ranked hub lipids (C, E) and GO terms through LION (D, F) in each module. (G and H) Representative images of immunostaining for ABCA7 and an ER marker KDEL in the cortex (G) and hippocampus of 5×FAD; control and 5×FAD; n*Abca7*$^{-/-}$ mice. Scale bar, 10 μm. ER, endoplasmic reticulum; GO, gene ontology; MEblack, upregulated module; MEtan downregulated module; PCA, principal component analysis; WGCNA, weighted correlation network analysis.

in n*Abca7*$^{-/-}$ mice compared with the controls (Table S15 and S16). In MElightyellow, *Exd2* and *Elavl4*, which are associated with mitochondria function,[62,63] were identified as the top two hub genes and were enriched for GO terms related to synapse function (Figure S12C). Significant differences in the protein levels of ETC complexes were not detected between the two groups (Figure S12D-E).

SnRNA-seq was also performed on frozen hemisphere samples from 5×FAD; n*Abca7*$^{-/-}$ and littermate 5×FAD control mice at 10 to 12 months of age. We identified 3776 single nuclei, then manually clustered these nuclei using the "FindNeighbors" and "FindClusters" functions in the Seurat package. There were no evident differences in cell proportions between the two groups (Figure S13A–C). Because *Abca7* expression mainly decreased in the excitatory neuron (ExN) rather than inhibitory neuron (InN) populations (Figure S13D), we first enriched GO biological process terms in the ExN cluster using REVIGO. We found GO terms related to phospholipid metabolism, such as "*phospholipid catabolic process*" and "*glycerophospholipid biosynthetic process*," were upregulated in the 5×FAD; n*Abca7*$^{-/-}$ mice compared to control groups (Figure S13E). On the other hand, downregulated GO terms were enriched for the pathways related to mitochondria, synapse, and apoptosis, including "*establishment of mitochondrion localization*," "*proton motive force-driven mitochondrial ATP synthesis*," "*translation at*

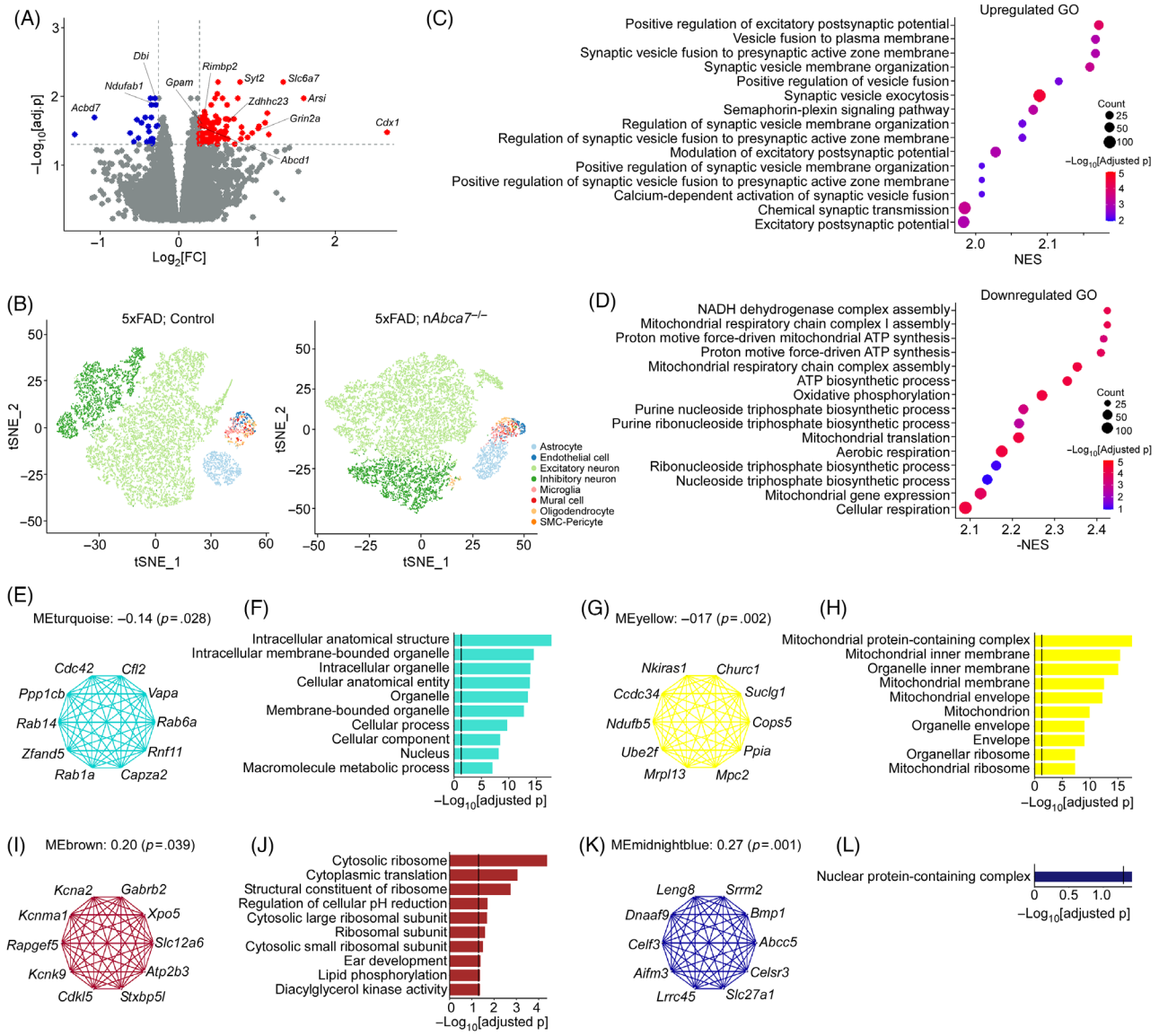

FIGURE 4 Neuronal ABCA7 deficiency alters brain transcriptomes in 10-month-old 5×FAD mice. (A) Volcano plot of DEG in bulk RNA-seq dataset of cortex comparing 5×FAD; n*Abca7*$^{-/-}$ mice (male, $N = 8$; female, $N = 7$) with 5×FAD control mice (male, $N = 4$; female, $N = 5$) at age of 10 months. (B) tSNE plot of bulk RNA-seq dataset by deconvolution. (C and D) GSEA of top 15 upregulated (C) and downregulated (D) pathways in bulk RNA-seq dataset comparing 5×FAD; n*Abca7*$^{-/-}$ mice with 5×FAD control mice. (E–L) WGCNA in bulk RNA-seq dataset with two downregulated modules (MEturquoise and MEyellow) and two downregulated modules (MEbrown and MEmidnightblue) comparing 5×FAD; n*Abca7*$^{-/-}$ mice with 5×FAD control mice. Top-ranked hub genes (E, G, I, and K) and GO terms (F, H, J, and L) in each module. DEG, differentially expressed gene; GSEA, gene set enrichment analysis; WGCNA, weighted correlation network analysis; tSNE, t-stochastic nearest neighbors.

synapse," and "*negative regulation of neuron apoptotic process*" (Figure S13E). In the ExN cluster, 456 DEGs were identified with an adjusted p-value < 0.05 and |fold change| > 1.2 (Table S17). The heatmap shows DEGs related to the ABC transporter family (*Abca7*, *Abcf4*, *Abcb10*, and *Abca4*), mitochondria (*Tomm20*, *Ndufs2*, *Atp5a1*, *Atp5b*, *Atp5l*, *Atp5o*, and *Cox17*), apoptosis (*Casp7*, *Bnip2*, and *Bag1*), synapse (*Slc1a3*, *Rpl26*, and *Rps7*), and lipid metabolism (*Gpam*, *Pon2*, and *Hacl1*) (Figure S13F). Furthermore, we identified 24 upregulated GO terms and 315 downregulated GO terms with a p value < 0.05 in the cluster. Consistent with the results from bulk RNA-seq, the downregulated and upregulated GO terms were associated with the synaptic vesicle membrane, transmembrane transporter activity, and ATP-synthase complex/activity (Figures S13G and S13H and Table S18). Taken together, both bulk RNA-seq and snRNA-seq indicated that neuronal ABCA7 deficiency influenced brain transcriptome profiles related to mitochondrial and synaptic dysfunctions, particularly in ExNs.

3.5 | Downregulated mitochondria-related genes in brains of neuronal ABCA7-deficient 5×FAD mice

When we focused on mitochondria-related genes in the bulk RNA-seq dataset, we found downregulation of genes encoding mitochondrial respiration chain-related molecules, especially mitochondrial complex

I (CI) and complex V (CV), in 5×FAD; n*Abca7*$^{-/-}$ mice compared to controls (Figure 5A). RT-qPCR confirmed the decreased mRNA levels of CI-related genes such as *Ndufaf1*, *Ndufa5*, and *Ndufc1* (Figure 5B–E) in the cortex of 10- to 12-month-old 5×FAD; n*Abca7*$^{-/-}$ mice, although those of mitochondrial fusion and fission-associated genes (*Mfn1*, *Mfn2*, *Mff*, *Fis1*, and *Opa1*) were not affected (Figure 5F–J). Consistently, immunostaining revealed a reduction in NDUFAB1 expression in the cortex of 5×FAD; n*Abca7*$^{-/-}$ mice (Figure 5K). In addition, we also examined the amounts of mitochondrial fusion proteins (MFN2 and OPA1) and fission proteins (FIS1 and DRP1) in the cortical samples by Western blotting (Figure 5L). We found decreased MFN2 but increased FIS1 in the 5×FAD; n*Abca7*$^{-/-}$ mice compared to controls (Figures 5L and 5M). While altered mitochondrial dynamics are associated with apoptosis,[64] we found increased cleaved caspase-8 protein levels in the cortex of 5×FAD; n*Abca7*$^{-/-}$ mice (Figure 5M). We could not observe those differences in mitochondrial molecules in the cortex of 10- to 12-month-old n*Abca7*$^{-/-}$ mice without amyloid pathology (Figure S14).

3.6 | Disturbed synaptic mitochondria function in neuronal ABCA7-deficient 5×FAD mice

Synaptic activity heavily depends on mitochondrial OXPHOS via the ETC.[24,27] To investigate the role of neuronal ABCA7 in synaptic mitochondria, we isolated synaptosomes from the brains of 5×FAD; n*Abca7*$^{-/-}$ and littermate 5×FAD; control mice aged 10 to 12 months (Figure 6A). Western blotting revealed an enrichment of synaptic proteins, including PSD95, SYP, and SNAP25, in synaptosomes from both groups of mice. We also found higher levels of ABCA7, IMM marker TIM23, and outer mitochondrial membrane marker TOM20 in the synaptosomes than in the cytosolic fractions (Figure 6A). To investigate the functional aspects of synaptic mitochondria, we measured the OCR in isolated synaptosomes using a Seahorse XF96 analyzer. We found diminished OCR in basal respiration, maximum respiration, proton leak, non-mitochondrial oxygen consumption, and spare respiratory capacity of synaptosomes from 5×FAD; n*Abca7*$^{-/-}$ mice compared to controls (Figure 6B–H). Furthermore, Western blotting revealed reductions in the mitochondrial CI marker NDUFAB8 and CV marker ATP5A in isolated synaptosomes from 5×FAD; n*Abca7*$^{-/-}$ mice compared to controls (Figure 6I–J), consistent with the results from transcriptomics. There were no evident differences in mitochondrial respiration and ETC protein levels in synaptosomes between 5×FAD; n*Abca7*$^{-/-}$ mice and the controls at 4 to 5 months old (Figure S15) as well as between n*Abca7*$^{-/-}$ and the controls at 10 to 12 months old (Figure S16).

Cytochrome c release from mitochondria is associated with apoptosis[64] and shuttles electrons for the respiratory chain at the mitochondrial intermembrane.[65] We found reduced interactions between cytochrome c and the ETC complexes in synaptosomes isolated from 5×FAD; n*Abca7*$^{-/-}$ mice by immunoprecipitation of cytochrome c (Figure 6K). Consistently, immunoprecipitation with TIM23 antibody also showed that TIM23-associated cytochrome c at the mitochondrial intermembrane was reduced in 5×FAD; n*Abca7*$^{-/-}$ mice (Figure 6L). These results implied that neuronal ABCA7 deficiency enhanced cytochrome c release from synaptic mitochondria, resulting in neuronal apoptosis. We also found that synaptosomes from the 5×FAD; n*Abca7*$^{-/-}$ mice contained more Aβ (Figure 6M), which may contribute to exacerbated synaptic mitochondria dysfunction.

Furthermore, we performed lipidomics on synaptosomes from the brains of 5×FAD; n*Abca7*$^{-/-}$ and littermate 5×FAD control mice aged 10 to 12 months. Although CL18:1-18:1-18:1-18:1 was reduced in 5×FAD; n*Abca7*$^{-/-}$ mice compared to controls, we found upregulations of PC and cholesteryl ester (CE) subclasses (Figure 6N). In addition, two upregulated modules (MEyellow and MEred) were identified through WGCNA in lipidomics by comparing 5×FAD; n*Abca7*$^{-/-}$ with the controls (Table S19). Hub lipids in MEyellow were enriched for PC species and top-ranked pathways included "*neutral intrinsic curvature*" (Figures 6O and 6P). MEred included various CE species (Figures 6Q and 6R) that were not identified through bulk lipidomics in mouse brains. Thus, neuronal ABCA7 deficiency may cause abnormal CE accumulation specifically in the synaptic membranes, vesicles, and mitochondria.

3.7 | Effects of differential ABCA7 expression on transcriptomes in AD brains

To validate the findings from our mouse models, we utilized the snRNA-seq dataset from the ROSMAP and SEA-AD cohort (syn26223298). In the ROSMAP dataset, we obtained all AD participants with *APOE* ε3/ε3 and Braak stages V–VI, followed by the assessment for *ABCA7* expression in neuronal populations as a pseudobulk RNA-seq using the existing annotation in the datasets. Finally, we selected AD cases with the highest *ABCA7* expression (*ABCA7*^{high}; $N = 6$) and lowest *ABCA7* expression (*ABCA7*^{low}; $N = 6$) (Table S1). *ABCA7*^{high} and *ABCA7*^{low} groups included 14,968 and 8002 cells, respectively, with nine clusters including ExN and InN (Figure 7A–C). Pseudobulk RNA-seq confirmed that *ABCA7* expression was lower in both ExN and InN of *ABCA7*^{low} group than those of the *ABCA7*^{high} group (Figure 7D). In the ExN cluster, "*synaptic vesicle maturation*" and "*respiratory electron transport chain*" were identified in the upregulated GO terms by comparing the *ABCA7*^{low} group with the *ABCA7*^{high} group, while "*positive regulation of synaptic transmission*" and "*positive regulation of CREB transcription factor activity*" were identified in downregulated GO terms (Figures 7E and 7F and Table S20), suggesting the association of neuronal ABCA7 expression with mitochondrial and synaptic functions. In the InN cluster, one downregulated GO term related to lipid transportation and localization was identified (Figure 7F and Table S20). We also obtained the dataset from all AD cases with Braak stages V and VI from the SEA-AD dataset. We selected AD cases with the highest *ABCA7* expression (*ABCA7*^{high}; $N = 10$) and lowest *ABCA7* expression (*ABCA7*^{low}; $N = 10$) (Table S2) by assessing *ABCA7* expression in neuronal populations as a pseudobulk RNA-seq using the existing annotation in the datasets. *ABCA7*^{high} and *ABCA7*^{low} groups included 149,302 and 125,992 cells, respectively, with eight clusters including ExN1, ExN2,

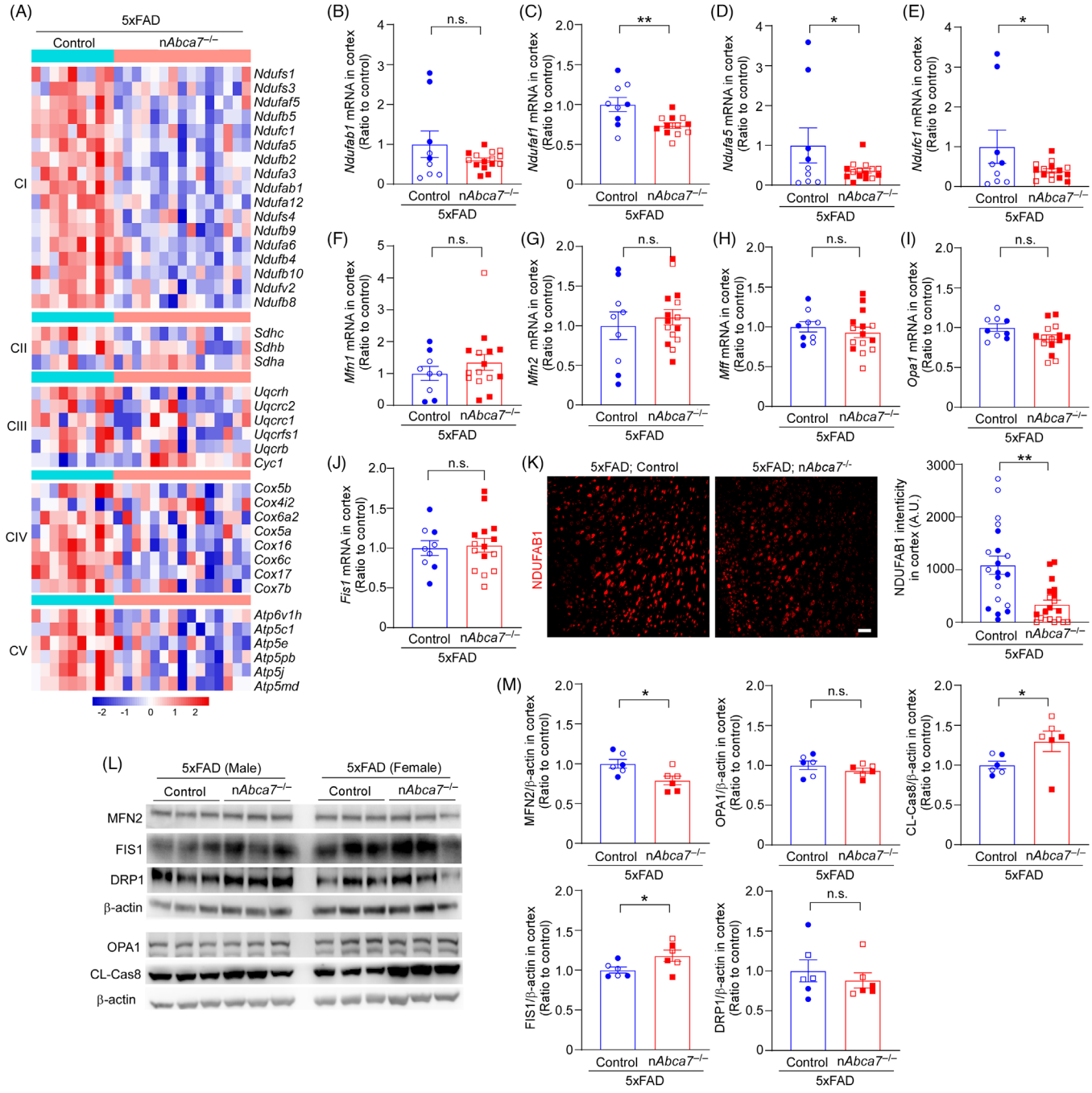

FIGURE 5 Neuronal ABCA7 deficiency reduces brain expressions of mitochondrial respiratory genes in 10- to 12-month-old 5×FAD mice. (A) Heatmap of mitochondrial respiratory genes in bulk RNA-seq dataset of cortex from 5×FAD control and 5×FAD; n*Abca7*$^{-/-}$mice. (B–J) mRNA expressions of mitochondria-related genes measured by RT-qPCR in cortex from 5×FAD; control (male, $N = 4$; female, $N = 5$) and 5×FAD; n*Abca7*$^{-/-}$ mice (male, $N = 6$ to 8; female, $N = 6$ -ETC, electron transport chain; SYP, synaptophysin; GO, Gene Ontology; WGCNA, weighted correlation network analysis; n.s., not significant. 7). (K) Quantification of NDUFFAB1 positivity by immunostaining in cortex of 5×FAD control (male, $N = 10$; female, $N = 10$) and 5×FAD; n*Abca7*$^{-/-}$ mice (male, $N = 10$; female, $N = 10$). Scale bars, 50 μm. (L and M) Quantification of mitochondria-related proteins by Western blotting in cortex from 5×FAD control (male, $N = 3$; female, $N = 3$) and 5×FAD; n*Abca7*$^{-/-}$ mice (male, $N = 3$; female, $N = 3$). Data are shown in mean ± SEM. Open and closed symbols indicate female and male mice, respectively. $^{*}p < 0.05$, $^{**}p < 0.01$, and n.s. by two-way ANOVA after adjusting for sex. n.s., not significant.

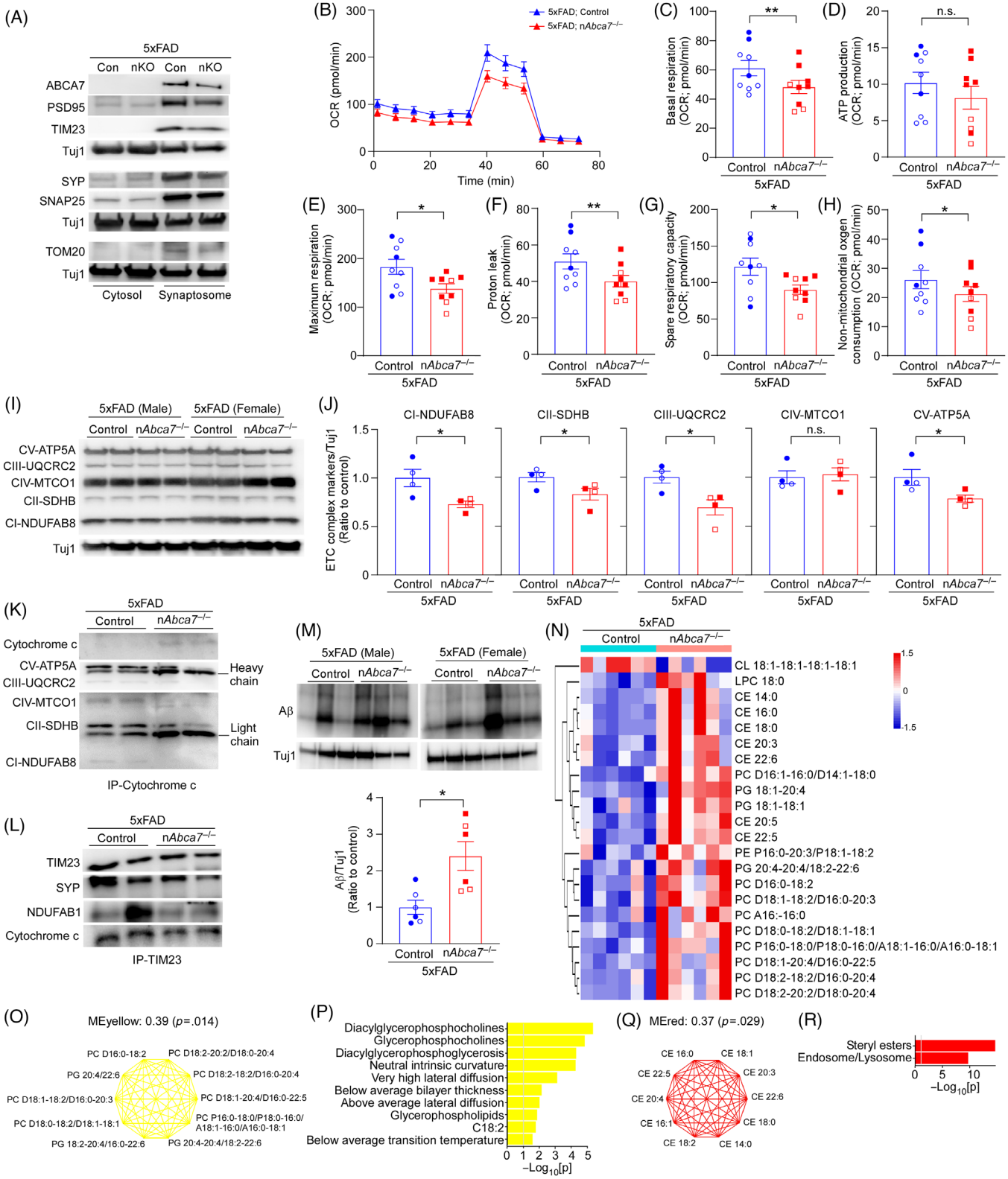

FIGURE 6 Neuronal ABCA7 deficiency disturbs synaptic mitochondrial function in 10- to 12-month-old 5×FAD mice. (A) Western blotting images for ABCA7, mitochondrial marker proteins (Tim23 and TOM20), and synaptic marker proteins (PSD95, SYP, and SNAP25) in the synaptosomes isolated from 5×FAD; control and 5×FAD; n*Abca7*$^{-/-}$ mice. (B–H) Mitochondrial respiration measured by Mito Stress Test Kit through Seahorse XFe96 extracellular flux analyzer in synaptosomes isolated from 5×FAD control (male, $N = 3$; female, $N = 6$) and 5×FAD; n*Abca7*$^{-/-}$ mice (male, $N = 6$; female, $N = 3$). (I and J) Quantification of ETC complexes by Western blotting using a cocktail antibody kit in synaptosomes isolated from 5×FAD control (male, $N = 2$; female, $N = 2$) and 5×FAD; n*Abca7*$^{-/-}$ mice (male, $N = 2$; female, $N = 2$). (K and L) Immunoprecipitation with cytochrome c for ETC complexes (K) and immunoprecipitation with TIM23 for SYP, NDUFAB1, and cytochrome c (L) in synaptosomes isolated from 5×FAD control and 5×FAD; n*Abca7*$^{-/-}$ mice. (M) Quantification of Aβ by Western blotting in synaptosomes isolated

and InN (Figure S17A–C). Pseudobulk RNA-seq revealed that *ABCA7* expression was significantly different in ExN2, but not in ExN1 or InN, between the two groups (Figure S17D). In the ExN1 cluster, "*release of cytochrome c from mitochondria*" and "*regulation of phospholipid catabolic process*" were identified in the upregulated GO terms by comparing the *ABCA7*^{low} group with the *ABCA7*^{high} group, while myelin-related and vesicle-related GOs were downregulated (Figure S17E and Table S21). In the ExN2 cluster, the upregulated GO terms included "*post-synaptic neurotransmitter receptor internalization*," "*vesicle localization*," "*apoptotic signaling pathway*," "*membrane organization*," and "*phospholipid translocation*," consistent with the results from mouse models. In contrast, downregulated GO terms were enriched for pathways related to myelin formation, lipoprotein particle organization, and ER regulation (Figure S17F and Table S21). Next, we investigated the synaptic and mitochondrial protein levels in *post mortem* AD brain samples (N = 20) (Table S3). ABCA7 levels were measured by Western blotting. The cohort was divided into two groups based on the ABCA7 levels (ABCA7^{high} and ABCA7^{low}). Consistent with our findings in the mouse models, SNAP25, PSD95, TIM23, and ATP5A levels were significantly lower in the ABCA7^{low} group than in the ABCA7^{high} group (Figure 7H–I).

4 | DISCUSSION

Previous studies showed that ABCA7 deficiency aggravated AD-related phenotypes in various amyloid model mice.[16–18] Further, a neuropathological study showed that lower brain ABCA7 protein levels were associated with earlier development of AD pathology.[66] In this study, for the first time, we demonstrated that deletion of neuronal ABCA7 exacerbated Aβ pathology, neuronal damage, and mitochondrial dysfunction using neuron-specific ABCA7 KO mice with 5×FAD background. Although ABCA7 in microglia plays a role in brain Aβ clearance,[16,19] our findings revealed that neuronal ABCA7 deficiency was sufficient to increase brain Aβ accumulation, suggesting multiple mechanisms by which ABCA7 modulates AD pathology.

ABC transporters constitute a superfamily of highly conserved proteins involved in the membrane transport of various substrates, such as amino acids, lipids, and sterols, across cell membranes.[67] Indeed, our lipidomics study revealed that neuronal ABCA7 deficiency modulated lipid profiles in mouse brains. Subclasses of PE and PC were particularly increased in the brains and synaptosomes of 5×FAD; n*Abca7*$^{-/-}$ mice. Since lipid compositions of the cellular membrane influence endocytosis and trafficking between organelles,[68] the altered membrane lipid profiles caused by ABCA7 deficiency may accelerate APP endocytosis subsequent to β-cleavage in neurons.[18] Additionally, higher PE levels are likely to be associated with increased γ-secretase activity.[69] Thus, neuronal ABCA7 deficiency may increase Aβ generation through multiple mechanisms. While PC is a major phospholipid class in the outer leaflet of plasma membrane,[70] the interaction of Aβ with the plasma membrane induces its conformational change to aggregates.[71] Thus, Aβ seeding may be exacerbated by unbalanced PC components in neuronal plasma membranes in 5×FAD; n*Abca7*$^{-/-}$ mice. When internalized into neurons, Aβ aggregates possibly propagate across the synapse to connected neurons.[72] As we also found an increase in Aβ in synaptosomes isolated from 5×FAD; n*Abca7*$^{-/-}$ mice, neuronal ABCA7 deficiency may result in facilitated transneuronal propagation of Aβ, although further studies are needed.

Bulk RNA-seq revealed that neuronal ABCA7 deficiency induced the downregulation of the mitochondrial ETC, especially complex I (CI) of the OXPHOS pathway, in the cortex of 5×FAD mice. SnRNA-seq also revealed that pathways related to ATPase regulator activity, ATP synthase complex, and ATP synthase complex were predominantly downregulated in ExNs in 5×FAD; n*Abca7*$^{-/-}$ mice compared to 5×FAD control mice. Consistently, diminished mitochondrial respiration and reduced levels of complex I, II, III, and V marker proteins were detected in synaptosomes isolated from 5×FAD; n*Abca7*$^{-/-}$ mice. Increasing evidence indicates that disturbances in the OXPHOS pathway are hallmarks of AD brains.[73–76] Altered mitochondrial morphology, dynamics, and transport have been implicated in AD brains and mouse models.[77–80] Since neuronal activity has a high-energy demand, mitochondrial dysregulation due to ABCA7 deficiency may make neurons vulnerable to Aβ toxicity, which is supported by exacerbated dystrophic neurites and increased plasma NfL levels in 5×FAD; n*Abca7*$^{-/-}$ mice. It is also possible that Aβ accumulation in synapse facilitated by ABCA7 deficiency further disrupts mitochondrial functions[81,82] in 5×FAD; n*Abca7*$^{-/-}$ mice as synaptic mitochondrial dysfunction became apparent only in the presence of abundant Aβ deposition in our mouse models. We also found that synaptic and mitochondrial protein levels were lower in AD brains with low ABCA7 expression than in those with high ABCA7 expression. Nonetheless, bulk RNA-seq revealed that neuronal ABCA7 deficiency was associated with the downregulation of synapse assembly pathways but upregulation of ATP synthesis pathways in mouse brains without amyloid pathology, while major mitochondria-associated molecules levels were not affected. Consistently, the snRNA-seq dataset from the ROSMAP cohort identified the downregulation of mitochondrial ETC pathways in ExN clusters when comparing the lower ABCA7 group with the higher group. Since OXPHOS activity increases in the hippocampus of early symptomatic *App* knock-in mice accompanied by ROS production,[83] these

from 5×FAD control (male, N = 3; female, N = 3) and 5×FAD; n*Abca7*$^{-/-}$ mice (male, N = 3; female, N = 3). (N) Hierarchical clustering of differentially expressed lipids with p <0.05 by two-way ANOVA after adjusting for sex in synaptosomes from 5×FAD control (male, N = 3; female, N = 3) and 5×FAD; n*Abca7*$^{-/-}$ mice (male, N = 3; female, N = 3). (O–R) WGCNA in lipidomics dataset in synaptosomes with two upregulated modules (MEred and MEyellow) comparing 5×FAD; n*Abca7*$^{-/-}$ mice with 5×FAD control mice. Top-ranked hub lipids (O, Q) and GO terms through LION (P, R) in each module. Data are shown in mean ± SEM. Open and closed symbols indicate female and male mice, respectively. *p <0.05, **p <0.01, and n.s. by two-way ANOVA after adjusting for sex. ETC, electron transport chain; GO, Gene Ontology; n.s., not significant; SYP, synaptophysin; WGCNA, weighted correlation network analysis.

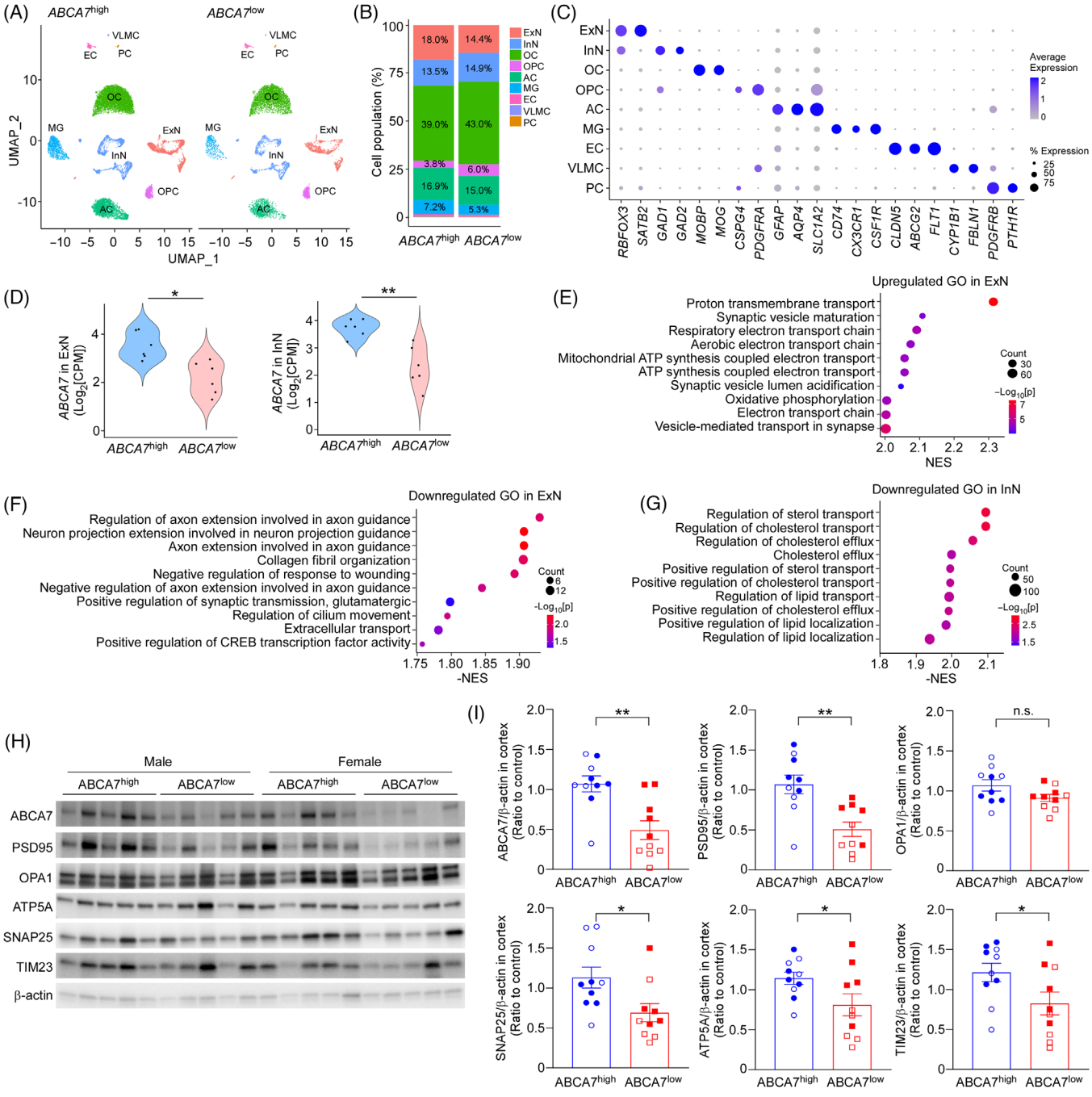

FIGURE 7 *ABCA7* expression influences neuronal transcriptomes in AD brains from ROSMAP. (A–C) UMAP showing clusters of single nucleus events captured in snRNA-seq dataset from AD patients' prefrontal cortices with high (male, $N = 3$; female, $N = 3$) and low (male, $N = 3$; female, $N = 3$) *ABCA7* expression in neuronal populations (A). Bar chart showing cell proportions (B). Annotation markers for each brain cell population (C). ExN, InN, OC, OPC, AC, MG, EC, VLMC. (D) *ABCA7* expression in clusters of ExN and InN clusters; $^{*}p < 0.05$ and $^{**}p < 0.01$ by adjusting sex and cell counts. (E and G) Upregulated (E) and downregulated GOs (F) of GSEA in ExN. (G) Only downregulated GOs were detected in InN. (H and I) Synaptic (PSD95 and SNAP25) and mitochondrial (OPA1, ATP5A, and TIM23) protein markers measured by Western blotting in AD brains with high (male, $N = 5$; female, $N = 5$) and low (male, $N = 5$; female, $N = 5$) ABCA7 expression. Data are shown in mean ± SEM. Open and closed symbols indicate females and males, respectively. $^{*}p < 0.05$, $^{**}p < 0.01$, and n.s. by two-way ANOVA after adjusting for sex. AC, astrocyte; AD, Alzheimer's disease; ExN, excitatory neuron; EC, endothelial cell; GO, Gene Ontology; InN, inhibitory neurons; MG, microglia; n.s., not significant; OC, oligodendrocytes; OPC, oligodendrocyte precursor cells; PC, pericyte; VLMC, vascular leptomeningeal cell.

transcriptome signatures may also indicate the contribution of ABCA7 to mitochondria and synapse homeostasis. In addition, the snRNA-seq dataset from the SEA-AD cohort identified "*release of cytochrome c from mitochondria*" and "*apoptotic mitochondrial changes*" as major upregulated pathways in ExNs of the lower ABCA7 expression group. While cytochrome c transfers electrons from complex III to complex IV under normal conditions, it is released from the mitochondria during apoptosis.[65] Our previous study showed that neuronal ABCA7 deficiency led to a reduction in synaptic proteins and altered mitochondrial morphology in synaptosomes from aged mice without amyloid pathology.[22] Thus, ABCA7 dysfunction and/or a reduction in neurons may aggravate neuronal damage during the development of various age-related neurodegenerative conditions, including AD.

ABCA7 is localized to the ER, plasma membrane, and other cellular organelles in HEK cells, whereas ABCA7 with AD risk mutants is predominantly detected in the ER.[84] As the ER and mitochondria are central organelles that regulate lipid metabolism, exogenous phosphatidic acid excessively accumulates in the ER in ABCA7-deficient induced pluripotent stem cell-derived neurons.[22] We also identified "*phospholipid translocation*" as one of the top-ranked pathways influenced by ABCA7 levels in the snRNA-seq dataset from AD brains. Therefore, proper intracellular trafficking of ABCA7 may be necessary to maintain the homeostasis of lipid synthesis and distribution from the ER to other compartments in neurons. In 5×FAD; n*Abca7*$^{-/-}$ mice, we found that CL 18:1-18:1-18:1-18:1-18:1 was reduced in synaptosomes compared with the control group, although other minor CL subclasses were rather increased in the brain. CL is the main inner mitochondria membrane phospholipid that plays a critical role in mitochondrial metabolism[85,86] and dynamics.[87] CL can influence ETC complexes and interact with pro-apoptotic enzymes to induce programmed cell death.[88] A decrease in CL likely reduces the binding affinity of cytochrome c to the mitochondrial membrane.[89,90] Thus, dysregulation of CL metabolism caused by ABCA7 deficiency may be a central pathway that triggers mitochondrial damage and subsequent apoptosis in neurons. In addition, we observed increased CE subclass levels in synaptosomes isolated from 5×FAD; n*Abca7*$^{-/-}$ mice. CE is the main neutral lipid in lipid droplets budding from the ER.[91] During aging and AD development, increased lipid droplet formation has been detected in various brain cell types, including neurons.[92] Thus, the increase in CE species in synaptosomes may be a consequence of altered ER/mitochondria lipid metabolism due to ABCA7 deficiency. While lipid droplets play protective roles against ER stress and mitochondria damage, excess lipid accumulation beyond the storage capacity causes lipotoxicity.[91] Of note, neuronal ABCA7 deficiency more predominantly influenced brain lipidomes in mice without amyloid pathology compared to those with 5×FAD background. We found that total levels of CL, PA, PI, and PS were significantly reduced in n*Abca7*$^{-/-}$ mice compared to controls. Thus, the lipid dysmetabolism induced by neuronal ABCA7 deficiency may be a triggering event prior to the development of mitochondrial dysregulation and synaptic damage, although further studies are needed.

In summary, our results demonstrate that the ABCA7 loss-of-function in neurons is associated with a heightened manifestation of AD pathogenesis, particularly marked by mitochondrial and synaptic dysfunction as well as Aβ pathology. These findings provide valuable insights into the intricate molecular processes underlying the development of AD and emphasize the significant role of ABCA7 in maintaining proper neuronal function and lipid metabolism. Moreover, our study suggests that interventions aimed at restoring ABCA7 function and lipid homeostasis in neurons hold promise as potential therapeutic strategies for AD. Because ABCA7 is expressed in various brain cell types, future studies are needed to define the cell-type-specific contributions of ABCA7 to AD-related phenotypes.

AUTHOR CONTRIBUTIONS

Ni Wang, Guojun Bu, and Takahisa Kanekiyo designed the research studies. Ni Wang, Skylar C. Starling, Devon H. Haskell, Astrid C. Quintero, Keiji Kawatani, Yasuteru Inoue, Francis Shue, Xiaoye Ma, Tomonori Aikawa, Yuka A. Martens, Aishe Kurti, Tammee M. Parsons, Ralph B. Perkerson, Bhaskar Roy, and Ana-Caroline Raulin conducted experiments and acquired data. Ni Wang, Yining Pan, Yingxue Ren, Hanmei Bao, and Xianlin Han analyzed lipidome and/or RNA-seq data. Michael DeTure and Dennis W. Dickson dissected and provided *post mortem* human brain samples. Ni Wang, Yining Pan, and Takahisa Kanekiyo analyzed all data. Ni Wang, Yining Pan, and Takahisa Kanekiyo wrote the first draft. All authors contributed to writing the final manuscript.

ACKNOWLEDGMENTS

The results of human snRNA-seq are in part based on data obtained from the AD Knowledge Portal (https://adknowledgeportal.org/). Study data were generated from *post mortem* brain tissue provided by the Religious Orders Study and Rush Memory and Aging Project (ROSMAP) cohort at Rush Alzheimer's Disease Center, Rush University Medical Center, Chicago. Study data were generated from *post mortem* brain tissue obtained from the University of Washington BioRepository and Integrated Neuropathology (BRaIN) laboratory and Precision Neuropathology Core. We thank all the participants in our study. We also thank Dr. Owen Ross for supporting human snRNA-seq analysis. This work was supported by NIH grants RF1AG081203, U19AG069701, R01AG071226, RF1AG057181, and RF1AG068034 (to T.K.), RF1AG081203, P30AG013319, and P30 AG044271 (to X.H.), and P30AG062677 (to D.W.D.) and a Cure Alzheimer's Fund grant (to T.K.). The results of human snRNA-seq from the ROSMAP cohort at Rush Alzheimer's Disease Center was funded by NIH grants U01AG061356 (De Jager/Bennett), RF1AG057473 (De Jager/Bennett), and U01AG046152 (De Jager/Bennett) as part of the AMP-AD consortium, as well as NIH grants R01AG066831 (Menon) and U01AG072572 (De Jager/St George-Hyslop). Study data were generated from *post mortem* brain tissue obtained from the University of Washington BioRepository and Integrated Neuropathology (BRaIN) laboratory and Precision Neuropathology Core, which is supported by NIH grants for the UW Alzheimer's Disease Research Center (P50AG005136 and P30AG066509) and the Adult Changes in Thought Study (U01AG006781 and U19AG066567). The human snRNA-seq is supported by NIA grant U19AG060909

CONFLICT OF INTEREST STATEMENT

T.K. has served on scientific advisory boards for Path Biotech LLC and has consulted for Ono Pharma Inc. G.B. serves as a consultant for SciNeuro Pharmaceuticals and Kisbee Therapeutics. Other authors declare no competing interests. Author disclosures are available in the supporting information.

CONSENT STATEMENT

We used exclusively deidentified human snRNA seq datasets from ROSMAP and SEA-AD cohorts and deidentified human brain samples from the Mayo Clinic Brain Bank. All participants signed informed and repository consent.

DATA AVAILABILITY STATEMENT

The RNA-seq data that support the findings of this study are deposited in the Gene Expression Omnibus repository under accession number GSE291092, GSE291086, and GSE291674. All other data are available from the corresponding author upon reasonable request.

REFERENCES

1. 2022 Alzheimer's disease facts and figures. *Alzheimers Dement*. 2022;18:700-789.
2. Cacace R, Sleegers K, Van Broeckhoven C. Molecular genetics of early-onset Alzheimer's disease revisited. *Alzheimers Dement*. 2016;12:733-748.
3. Wingo TS, Lah JJ, Levey AI, Cutler DJ. Autosomal recessive causes likely in early-onset Alzheimer disease. *Arch Neurol*. 2012;69:59-64.
4. Gatz M, Reynolds CA, Fratiglioni L, et al. Role of genes and environments for explaining Alzheimer disease. *Arch Gen Psychiatry*. 2006;63:168-174.
5. Strittmatter WJ, Saunders AM, Schmechel D, et al. Apolipoprotein E: high-avidity binding to beta-amyloid and increased frequency of type 4 allele in late-onset familial Alzheimer disease. *Proc Natl Acad Sci U S A*. 1993;90:1977-1981.
6. Hollingworth P, Harold D, Sims R, et al. Common variants at ABCA7, MS4A6A/MS4A4E, EPHA1, CD33 and CD2AP are associated with Alzheimer's disease. *Nat Genet*. 2011;43:429-435.
7. Lambert JC, Ibrahim-Verbaas CA, Harold D, et al. Meta-analysis of 74,046 individuals identifies 11 new susceptibility loci for Alzheimer's disease. *Nat Genet*. 2013;45:1452-1458.
8. Reitz C, Jun G, Naj A, et al. Variants in the ATP-binding cassette transporter (ABCA7), apolipoprotein E ε4,and the risk of late-onset Alzheimer disease in African Americans. *JAMA*. 2013;309:1483-1492.
9. Steinberg S, Stefansson H, Jonsson T, et al. Loss-of-function variants in ABCA7 confer risk of Alzheimer's disease. *Nat Genet*. 2015;47:445-447.
10. Cuyvers E, De Roeck A, Van den Bossche T, et al. Mutations in ABCA7 in a Belgian cohort of Alzheimer's disease patients: a targeted resequencing study. *Lancet Neurol*. 2015;14:814-822.
11. De Roeck A, Van den Bossche T, van der Zee J, et al. Deleterious ABCA7 mutations and transcript rescue mechanisms in early onset Alzheimer's disease. *Acta Neuropathol*. 2017;134:475-487.
12. Bellenguez C, Charbonnier C, Grenier-Boley B, et al. Contribution to Alzheimer's disease risk of rare variants in TREM2, SORL1, and ABCA7 in 1779 cases and 1273 controls. *Neurobiol Aging*. 2017;59:220.e1-e9.
13. Le Guennec K, Nicolas G, Quenez O, et al. ABCA7 rare variants and Alzheimer disease risk. *Neurology*. 2016;86:2134-2137.
14. Kaminski WE, Orso E, Diederich W, Klucken J, Drobnik W, Schmitz G. Identification of a novel human sterol-sensitive ATP-binding cassette transporter (ABCA7). *Biochem Biophys Res Commun*. 2000;273:532-538.
15. Abe-Dohmae S, Ikeda Y, Matsuo M, et al. Human ABCA7 supports apolipoprotein-mediated release of cellular cholesterol and phospholipid to generate high density lipoprotein. *J Biol Chem*. 2004;279:604-611.
16. Kim WS, Li H, Ruberu K, et al. Deletion of Abca7 increases cerebral amyloid-beta accumulation in the J20 mouse model of Alzheimer's disease. *J Neurosci*. 2013;33:4387-4394.
17. Satoh K, Abe-Dohmae S, Yokoyama S, St George-Hyslop P, Fraser PE. ATP-binding cassette transporter A7 (ABCA7) loss of function alters Alzheimer amyloid processing. *J Biol Chem*. 2015;290:24152-24165.
18. Sakae N, Liu CC, Shinohara M, et al. ABCA7 Deficiency Accelerates Amyloid-beta Generation and Alzheimer's Neuronal Pathology. *J Neurosci*. 2016;36:3848-3859.
19. Aikawa T, Ren Y, Yamazaki Y, et al. ABCA7 haplodeficiency disturbs microglial immune responses in the mouse brain. *Proc Natl Acad Sci U S A*. 2019;116:23790-23796.
20. Jehle AW, Gardai SJ, Li S, et al. ATP-binding cassette transporter A7 enhances phagocytosis of apoptotic cells and associated ERK signaling in macrophages. *J Cell Biol*. 2006;174:547-556.
21. Shulman JM, Chen K, Keenan BT, et al. Genetic susceptibility for Alzheimer disease neuritic plaque pathology. *JAMA Neurol*. 2013;70:1150-1157.
22. Kawatani K, Holm ML, Starling SC, et al. ABCA7 deficiency causes neuronal dysregulation by altering mitochondrial lipid metabolism. *Mol Psychiatry*. 2023;29(3):809-819.
23. Lev S. Nonvesicular lipid transfer from the endoplasmic reticulum. *Cold Spring Harb Perspect Biol*. 2012;4:a013300.
24. Osellame LD, Blacker TS, Duchen MR. Cellular and molecular mechanisms of mitochondrial function. *Best Pract Res Clin Endocrinol Metab*. 2012;26:711-723.
25. Wang W, Zhao F, Ma X, Perry G, Zhu X. Mitochondria dysfunction in the pathogenesis of Alzheimer's disease: recent advances. *Mol Neurodegener*. 2020;15:30.
26. Sheng M, Sabatini BL, Sudhof TC. Synapses and Alzheimer's disease. *Cold Spring Harb Perspect Biol*. 2012;4:a005777.
27. Cai Q, Tammineni P. Mitochondrial Aspects of Synaptic Dysfunction in Alzheimer's Disease. *J Alzheimers Dis*. 2017;57:1087-1103.
28. von Maydell D, Wright S, Bonner JM, et al. Single-cell atlas of ABCA7 loss-of-function reveals impaired neuronal respiration via choline-dependent lipid imbalances. *bioRxiv*. 2024. doi:10.1101/2023.09.05.556135
29. Oakley H, Cole SL, Logan S, et al. Intraneuronal beta-amyloid aggregates, neurodegeneration, and neuron loss in transgenic mice with five familial Alzheimer's disease mutations: potential factors in amyloid plaque formation. *J Neurosci*. 2006;26:10129-10140.
30. Casanova E, Fehsenfeld S, Mantamadiotis T, et al. A CamKIIalpha iCre BAC allows brain-specific gene inactivation. *Genesis*. 2001;31:37-42.
31. Ou-Yang MH, Kurz JE, Nomura T, et al. Axonal organization defects in the hippocampus of adult conditional BACE1 knockout mice. *Sci Transl Med*. 2018;10:eaao5620.
32. Shinohara M, Kanekiyo T, Yang L, et al. APOE2 eases cognitive decline during Aging: clinical and preclinical evaluations. *Ann Neurol*. 2016;79:758-774.
33. Oue H, Yamazaki Y, Qiao W, et al. LRP1 in vascular mural cells modulates cerebrovascular integrity and function in the presence of APOE4. *JCI Insight*. 2023;8:e163822.
34. Tachibana M, Holm ML, Liu CC, et al. APOE4-mediated amyloid-beta pathology depends on its neuronal receptor LRP1. *J Clin Invest*. 2019;129:1272-1277.
35. Selkoe DJ. Normal and abnormal biology of the beta-amyloid precursor protein. *Annu Rev Neurosci*. 1994;17:489-517.

36. Yang K, Han X. Accurate quantification of lipid species by electrospray ionization mass spectrometry - Meet a key challenge in lipidomics. *Metabolites*. 2011;1:21-40.
37. Molenaar MR, Jeucken A, Wassenaar TA, van de Lest CHA, Brouwers JF, Helms JB. LION/web: a web-based ontology enrichment tool for lipidomic data analysis. *Gigascience*. 2019;8:giz061.
38. Kalari KR, Nair AA, Bhavsar JD, et al. MAP-RSeq: mayo analysis pipeline for RNA sequencing. *BMC Bioinformatics*. 2014;15:224.
39. Hansen KD, Irizarry RA, Wu Z. Removing technical variability in RNA-seq data using conditional quantile normalization. *Biostatistics*. 2012;13:204-216.
40. Law CW, Chen Y, Shi W, Smyth GK. voom: Precision weights unlock linear model analysis tools for RNA-seq read counts. *Genome Biol*. 2014;15:R29.
41. Robinson MD, McCarthy DJ, Smyth GK. edger: a Bioconductor package for differential expression analysis of digital gene expression data. *Bioinformatics*. 2010;26:139-140.
42. Ritchie ME, Phipson B, Wu D, et al. Limma powers differential expression analyses for RNA-sequencing and microarray studies. *Nucleic Acids Res*. 2015;43:e47.
43. Yao Z, van Velthoven CTJ, Nguyen TN, et al. A taxonomy of transcriptomic cell types across the isocortex and hippocampal formation. *Cell*. 2021;184:3222-3241 e26.
44. Marquez-Galera A, de la Prida LM, Lopez-Atalaya JP. A protocol to extract cell-type-specific signatures from differentially expressed genes in bulk-tissue RNA-seq. *STAR Protoc*. 2022;3:101121.
45. Satija R, Farrell JA, Gennert D, Schier AF, Regev A. Spatial reconstruction of single-cell gene expression data. *Nat Biotechnol*. 2015;33:495-502.
46. Yu G, Wang LG, Han Y, He QY. Clusterprofiler: an R package for comparing biological themes among gene clusters. *OMICS*. 2012;16:284-287.
47. Langfelder P, Horvath S. WGCNA: an R package for weighted correlation network analysis. *BMC Bioinformatics*. 2008;9:559.
48. Lun AT, McCarthy DJ, Marioni JC. A step-by-step workflow for low-level analysis of single-cell RNA-seq data with Bioconductor. *F1000Res*. 2016;5:2122.
49. Zhou Y, Zhou B, Pache L, et al. Metascape provides a biologist-oriented resource for the analysis of systems-level datasets. *Nat Commun*. 2019;10:1523.
50. Supek F, Bosnjak M, Skunca N, Smuc T. REVIGO summarizes and visualizes long lists of gene ontology terms. *PLoS One*. 2011;6:e21800.
51. Bennett DA, Buchman AS, Boyle PA, Barnes LL, Wilson RS, Schneider JA. Religious Orders Study and Rush Memory and Aging Project. *J Alzheimers Dis*. 2018;64:S161-S89.
52. Lun ATL, Riesenfeld S, Andrews T, Dao TP, Gomes T, participants in the 1st Human Cell Atlas J, et al. EmptyDrops: distinguishing cells from empty droplets in droplet-based single-cell RNA sequencing data. *Genome Biol*. 2019;20:63.
53. Condello C, Yuan P, Schain A, Grutzendler J. Microglia constitute a barrier that prevents neurotoxic protofibrillar Abeta42 hotspots around plaques. *Nat Commun*. 2015;6:6176.
54. Norgren N, Rosengren L, Stigbrand T. Elevated neurofilament levels in neurological diseases. *Brain Res*. 2003;987:25-31.
55. Saunders A, Macosko EZ, Wysoker A, et al. Molecular Diversity and Specializations among the Cells of the Adult Mouse Brain. *Cell*. 2018;174:1015-1030 e16.
56. Van Hove JL, Saenz MS, Thomas JA, et al. Succinyl-CoA ligase deficiency: a mitochondrial hepatoencephalomyopathy. *Pediatr Res*. 2010;68:159-164.
57. Pujol C, Lebigot E, Gaignard P, et al. MPC2 variants disrupt mitochondrial pyruvate metabolism and cause an early-onset mitochondriopathy. *Brain*. 2023;146:858-864.
58. Sylvester JE, Fischel-Ghodsian N, Mougey EB, O'Brien TW. Mitochondrial ribosomal proteins: candidate genes for mitochondrial disease. *Genet Med*. 2004;6:73-80.
59. Sanchez-Caballero L, Guerrero-Castillo S, Nijtmans L. Unraveling the complexity of mitochondrial complex I assembly: A dynamic process. *Biochim Biophys Acta*. 2016;1857:980-990.
60. Anderson CM, Stahl A. SLC27 fatty acid transport proteins. *Mol Aspects Med*. 2013;34:516-528.
61. Xie Q, Lin T, Zhang Y, Zheng J, Bonanno JA. Molecular cloning and characterization of a human AIF-like gene with ability to induce apoptosis. *J Biol Chem*. 2005;280:19673-19681.
62. Hensen F, Moretton A, van Esveld S, Farge G, Spelbrink JN. The mitochondrial outer-membrane location of the EXD2 exonuclease contradicts its direct role in nuclear DNA repair. *Sci Rep*. 2018;8:5368.
63. van der Linden RJ, Gerritsen JS, Liao M, et al. RNA-binding protein ELAVL4/HuD ameliorates Alzheimer's disease-related molecular changes in human iPSC-derived neurons. *Prog Neurobiol*. 2022;217:102316.
64. Westermann B. Mitochondrial fusion and fission in cell life and death. *Nat Rev Mol Cell Biol*. 2010;11:872-884.
65. Garrido C, Galluzzi L, Brunet M, Puig PE, Didelot C, Kroemer G. Mechanisms of cytochrome c release from mitochondria. *Cell Death Differ*. 2006;13:1423-1433.
66. Lyssenko NN, Pratico D. ABCA7 and the altered lipidostasis hypothesis of Alzheimer's disease. *Alzheimers Dement*. 2021;17:164-74.
67. Higgins CF. ABC transporters: from microorganisms to man. *Annu Rev Cell Biol*. 1992;8:67-113.
68. Haucke V, Di Paolo G. Lipids and lipid modifications in the regulation of membrane traffic. *Curr Opin Cell Biol*. 2007;19:426-435.
69. Calzada E, Onguka O, Claypool SM. Phosphatidylethanolamine Metabolism in Health and Disease. *Int Rev Cell Mol Biol*. 2016;321:29-88.
70. Casares D, Escriba PV, Rossello CA. Membrane lipid composition: effect on membrane and organelle structure, function and compartmentalization and therapeutic avenues. *Int J Mol Sci*. 2019;20.
71. Sanderson JM. The association of lipids with amyloid fibrils. *J Biol Chem*. 2022;298:102108.
72. Eisele YS, Bolmont T, Heikenwalder M, et al. Induction of cerebral beta-amyloidosis: intracerebral versus systemic Abeta inoculation. *Proc Natl Acad Sci U S A*. 2009;106:12926-12931.
73. Manczak M, Park BS, Jung Y, Reddy PH. Differential expression of oxidative phosphorylation genes in patients with Alzheimer's disease: implications for early mitochondrial dysfunction and oxidative damage. *Neuromolecular Med*. 2004;5:147-162.
74. Mastroeni D, Khdour OM, Delvaux E, et al. Nuclear but not mitochondrial-encoded oxidative phosphorylation genes are altered in aging, mild cognitive impairment, and Alzheimer's disease. *Alzheimers Dement*. 2017;13:510-519.
75. Zhang L, Guo XQ, Chu JF, Zhang X, Yan ZR, Li YZ. Potential hippocampal genes and pathways involved in Alzheimer's disease: a bioinformatic analysis. *Genet Mol Res*. 2015;14:7218-7232.
76. Sorrentino V, Romani M, Mouchiroud L, et al. Enhancing mitochondrial proteostasis reduces amyloid-beta proteotoxicity. *Nature*. 2017;552:187-193.
77. Balietti M, Giorgetti B, Casoli T, et al. Early selective vulnerability of synapses and synaptic mitochondria in the hippocampal CA1 region of the Tg2576 mouse model of Alzheimer's disease. *J Alzheimers Dis*. 2013;34:887-896.
78. Wang X, Su B, Lee HG, et al. Impaired balance of mitochondrial fission and fusion in Alzheimer's disease. *J Neurosci*. 2009;29:9090-9103.
79. Guo L, Tian J, Du H. Mitochondrial dysfunction and synaptic transmission failure in Alzheimer's disease. *J Alzheimers Dis*. 2017;57:1071-1086.

80. Reddy PH. Abnormal tau, mitochondrial dysfunction, impaired axonal transport of mitochondria, and synaptic deprivation in Alzheimer's disease. *Brain Res*. 2011;1415:136-148.
81. Mungarro-Menchaca X, Ferrera P, Moran J, Arias C. Beta-amyloid peptide induces ultrastructural changes in synaptosomes and potentiates mitochondrial dysfunction in the presence of ryanodine. *J Neurosci Res*. 2002;68:89-96.
82. Keller JN, Lauderback CM, Butterfield DA, Kindy MS, Yu J, Markesbery WR. Amyloid beta-peptide effects on synaptosomes from apolipoprotein E-deficient mice. *J Neurochem*. 2000;74:1579-1586.
83. Naia L, Shimozawa M, Bereczki E, et al. Mitochondrial hypermetabolism precedes impaired autophagy and synaptic disorganization in App knock-in Alzheimer mouse models. *Mol Psychiatry*. 2023;28:3966-3981.
84. Bossaerts L, Hendrickx Van de Craen E, Cacace R, Asselbergh B, Van Broeckhoven C. Rare missense mutations in ABCA7 might increase Alzheimer's disease risk by plasma membrane exclusion. *Acta Neuropathol Commun*. 2022;10:43.
85. Dudek J. Role of Cardiolipin in Mitochondrial Signaling Pathways. *Front Cell Dev Biol*. 2017;5:90.
86. Basu Ball W, Neff JK, Gohil VM. The role of nonbilayer phospholipids in mitochondrial structure and function. *FEBS Lett*. 2018;592:1273-1290.
87. Kameoka S, Adachi Y, Okamoto K, Iijima M, Sesaki H. Phosphatidic acid and cardiolipin coordinate mitochondrial dynamics. *Trends Cell Biol*. 2018;28:67-76.
88. Rijken PJ, Houtkooper RH, Akbari H, et al. Cardiolipin molecular species with shorter acyl chains accumulate in Saccharomyces cerevisiae mutants lacking the acyl coenzyme A-binding protein Acb1p: new insights into acyl chain remodeling of cardiolipin. *J Biol Chem*. 2009;284:27609-27619.
89. Ott M, Robertson JD, Gogvadze V, Zhivotovsky B, Orrenius S. Cytochrome c release from mitochondria proceeds by a two-step process. *Proc Natl Acad Sci U S A*. 2002;99:1259-1263.
90. Schug ZT, Gottlieb E. Cardiolipin acts as a mitochondrial signalling platform to launch apoptosis. *Biochim Biophys Acta*. 2009;1788:2022-2031.
91. Olzmann JA, Carvalho P. Dynamics and functions of lipid droplets. *Nat Rev Mol Cell Biol*. 2019;20:137-155.
92. Ralhan I, Chang CL, Lippincott-Schwartz J, Ioannou MS. Lipid droplets in the nervous system. *J Cell Biol*. 2021;220:e202102136.

SUPPORTING INFORMATION

Additional supporting information can be found online in the Supporting Information section at the end of this article.

How to cite this article: Wang N, Pan Y, Starling SC, et al. Neuronal ABCA7 deficiency aggravates mitochondrial dysfunction and neurodegeneration in Alzheimer's disease. *Alzheimer's Dement*. 2025;21:e70112.
https://doi.org/10.1002/alz.70112